Nematicity and Competing Orders in Superconducting Magic-Angle Graphene

Yuan Cao[1,*], Daniel Rodan-Legrain[1], Jeong Min Park[1], Noah F. Q. Yuan[1], Kenji Watanabe[2], Takashi Taniguchi[3], Rafael M. Fernandes[4], Liang Fu[1], Pablo Jarillo-Herrero[1,*]

[1]Department of Physics, Massachusetts Institute of Technology, Cambridge, Massachusetts 02139, USA.

[2]Research Center for Functional Materials, National Institute for Materials Science, Namiki 1-1, Tsukuba, Ibaraki 305-0044, Japan.

[3]International Center for Materials Nanoarchitectonics, National Institute for Materials Science, Namiki 1-1, Tsukuba, Ibaraki 305-0044, Japan.

[4]School of Physics and Astronomy, University of Minnesota, Minneapolis, MN 55455, USA.

*Correspondence to: caoyuan@mit.edu, pjarillo@mit.edu

Abstract: Strongly interacting electrons in solid-state systems often display tendency towards multiple broken symmetries in the ground state. The complex interplay between different order parameters can give rise to a rich phase diagram. Here, we report on the identification of intertwined phases with broken rotational symmetry in magic-angle twisted bilayer graphene (TBG). Using transverse resistance measurements, we find a strongly anisotropic phase located in a 'wedge' above the underdoped region of the superconducting dome. Upon its crossing with the superconducting dome, a reduction of the critical temperature is observed. Furthermore, the superconducting state exhibits an anisotropic response to a direction-dependent in-plane magnetic field, revealing a nematic pairing state across the entire superconducting dome. These results indicate that nematic fluctuations might play an important role in the low-temperature phases of magic-angle TBG, and pave the way for using highly-tunable moiré superlattices to investigate intertwined phases in quantum materials.

One Sentence Summary: Magic-angle graphene exhibits competing quantum phases with broken rotational symmetry, a hallmark present in many exotic quantum materials.

Main Text:

Spontaneous symmetry breaking is a ubiquitous process that occurs at all length scales in nature (*1*), from the endowment of mass to elementary particles through the Higgs mechanism, the emergence of ferromagnetism and superconductivity in mesoscopic and macroscopic systems, all the way to the creation of stars and galaxies in the early universe. In a solid-state system, besides time-reversal and gauge symmetries, there are certain discrete symmetries imposed by the underlying crystal lattice. However, these symmetries can be spontaneously broken when many-body electron-electron interactions in the system are significant. Studying these broken-symmetry states is fundamental to elucidate the various phases in these many-body systems (*2*, *3*). One example is an electronic nematic phase, where the discrete rotational symmetry of the

lattice is spontaneously broken due to electron correlations, while lattice translational and time-reversal symmetries are preserved (*4*, *5*). The resulting anisotropy of the system is in turn manifested in the spin, charge, and lattice degrees of freedom, and can be measured via scattering, transport and scanning probe experiments (*6–11*).

When a correlated system has multiple broken-symmetry phases, their relationship often goes beyond mere competition, giving rise to a complex phase diagram of intertwined phases (*12–14*). For example, in the underdoped region of the phase diagram of certain cuprate superconductors, a depletion in the critical temperature T_c is found near $p \approx 1/8$, where p is the hole doping concentration(*15*). This observation is typically attributed to the competition between superconductivity and a stripe phase that has spin and/or charge ordering (*3*, *15*, *16*). Charge order and superconductivity may also intertwine to form a pair density-wave state (*13*, *17*). Another example of intertwined order is a nematic superconducting state, which simultaneously breaks lattice rotational and gauge symmetries. Nematic pairing states have been reported in certain iron pnictides and in doped Bi_2Se_3, as revealed by thermal, magnetic, and transport measurements (*18–24*), although their microscopic origin is still unclear.

The recent discovery of correlated insulator and superconducting behaviors (*25*, *26*) in two-dimensional (2D) graphene superlattices brings the possibility of studying correlated superconducting materials with unprecedented tunability and richness. Twisted 2D materials exhibit long-range moiré patterns in real space that can be tuned by the twist angle (Fig. 1A). In twisted bilayer graphene (TBG) near the first magic-angle $\theta \approx 1.1°$, the interlayer hybridization results in nearly-flat bands at low energies, in which the electrons are localized in real space (Fig. 1A) (*27–29*). Near half-filling of the nearly-flat bands, emergent correlated insulator behavior and superconductivity have been demonstrated (*25*, *26*, *30*). In this work we study the interplay between the superconducting phase and other many-body phases in magic-angle TBG. Compared to conventional materials, a major advantage of magic-angle TBG is that the band filling can be continuously tuned by electrostatic gating instead of chemical doping, so that different phases can be accessed in a single device.

In this article, we investigate the phase diagram of magic-angle TBG in detail, focusing particularly on anisotropic properties in the superconducting and normal phases. We uncover an anisotropic in-plane electrical transport in magic-angle TBG at low temperatures using longitudinal and transverse resistivity measurements. In addition, we reveal an anisotropic in-plane critical field and an anisotropic response of the superconducting critical current to an in-plane magnetic field. Our results show that magic-angle TBG can spontaneously break lattice rotational symmetry in both the normal and superconducting phases, although the anisotropic properties of these two states are manifested in different observables, suggesting that the origins of these two anisotropic states might be different.

Characterization of Magic-angle Graphene

Using the previously developed ‘tear and stack’ dry-transfer technique (*31*, *32*), we fabricate high quality encapsulated TBG devices with twist angles around the first magic angle $\theta \approx 1.1°$ (see Supplementary Materials and Fig. S1 for Landau fan diagram). The main devices we report about are devices A and B, with twist angles of $\theta = 1.09°$ and $\theta = 1.08°$, respectively. We also have a third device C with $\theta = 1.07°$ shown in the Supplementary Materials, which exhibits very similar behavior as devices A and B. The low-energy bands in TBG are four-fold degenerate

(due to spin and valley degrees of freedom) and can sustain an electron density of $n_s = 4/A$, where A is the area of a moiré unit cell. This density corresponds to filling four electrons or holes per moiré unit cell. Near the first magic angle, correlated states can form at integer electron fillings of the moiré superlattice, *i.e.* when $n = \pm n_s/4, \pm n_s/2, \pm 3n_s/4$. This is believed to be a consequence of the fact that the electronic interactions become comparable to the bandwidth of the nearly-flat bands. In the resistivity measurements of device A shown in Fig. 1B, we indeed find an enhancement of the resistivity ρ_{xx} at all these integer fillings. A superconducting dome is recognizable upon hole-doping of the $-n_s/2$ insulating state, at temperatures below 2.5 K. Fig. 1C shows the $\rho_{xx}(T)$ curves of device A and device B at their optimal doping levels (highest T_c), where T is the sample temperature. Both devices exhibit a T_c in the range of 2.5~3 K (at 50% normal resistance), which is among the highest in our MATBG devices (see. Fig. 1E). Figure 1D shows the evolution of the V-I curves with temperature. From the log-log plot shown in the inset, we can extract the Berezinskii-Kosterlitz-Thouless (BKT) transition temperature to be $T_{BKT} \approx 2.2$ K. Devices A and B have in fact some of the highest transition temperatures among all reported magic-angle TBG devices so far (see Table S1 and Fig. S4), as evident from the T_c statistics shown in Fig. 1E, as well as devices reported in the literature (*26*, *30*, *33*).

Anisotropic Behavior in the Normal Phase

Figs. 2A and 2B show the resistivity versus gate-induced density, n, and temperature, T, maps of devices A and B, respectively, in the vicinity of $-n_s/2$. We find that in both devices the $-n_s/2$ region of the phase diagram has a rather complicated structure. As can be seen in Figs. 2A and 2B, there are two resistive features in the normal state: one 'wedge'-like feature above the superconducting dome (near -1.5×10^{12} cm^{-2} for device A and -1.4×10^{12} cm^{-2} for device B) that bends at elevated temperatures, and one resistive feature on the right-hand side of the dome (near -1.3×10^{12} cm^{-2} for both devices). While the latter feature corresponds to the $-n_s/2$ state similar to the correlated states previously reported in magic-angle TBG (*25*, *26*, *30*, *33*), the wedge-like feature creates a noticeable 'kink' (*i.e.* decrease in T_c) where it intersects with the superconducting dome. To further probe the resistive wedge-like feature, we apply a small perpendicular magnetic field to fully suppress superconductivity, as shown in Figs. 2C and 2D. Line cuts of the resistivity versus temperature at the densities corresponding to the 'kinks' of T_c are compared in Figs. 2E and 2F for the two devices. It can be clearly seen that when superconductivity is suppressed, the resistive wedge-like feature turns insulating upon approaching zero temperature. A small magnetic field thus results in a superconductor-to-insulator transition at this density. In Fig. 2G, we show the gradual suppression of T_c by the perpendicular magnetic field from zero to 180 mT in device A. We find that above about 90 mT, the superconducting dome splits at $n \approx -1.54\times10^{12}$ cm^{-2} into two domes. This density approximately coincides with the density where the wedge-like feature extrapolates to zero temperature. The separated domes are centered at around -1.52×10^{12} cm^{-2} and -1.67×10^{12} cm^{-2} respectively. The position of the splitting point corresponds to 15±5% hole doping with respect to the correlated insulator state. These findings are reminiscent of the behavior in certain underdoped cuprates near 1/8 doping (*3*, *15*, *16*, *34*).

To gain more insight into the possible origin of the resistive wedge-like feature, we measure the transverse voltage across the sample at zero magnetic field, which gives us the transverse resistance $R_{xy} = V_y/I_x$ (*35*, *36*). In an anisotropic conductor in two dimensions, the 2-by-2 resistivity tensor has two diagonal components $\rho = \mathrm{diag}\{\rho_1, \rho_2\}$. If the major axis of the

anisotropy (usually one of the crystal axis) is not aligned with the reference frame of the tensor, the off-diagonal terms of the resistivity tensor are proportional to $(\rho_1 - \rho_2)\sin(2\theta)$, where θ is the angle between the anisotropy axis and the reference x-axis (see Supplementary Materials for derivation). As a result, when an electrical current I_x flows in the x direction, a transverse voltage V_y appears across the edges perpendicular to the y axis, giving a nonvanishing $R_{xy} = V_y/I_x \propto (\rho_1 - \rho_2)\sin(2\theta)$, as long as $\sin(2\theta) \neq 0$ and $\rho_1 \neq \rho_2$. The first condition is assumed to be true in our experiment, since the lattice orientation is random with respect to the sample edge. Consequently, a non-vanishing transverse resistance in our experiment implies anisotropic resistivity, $\rho_1 \neq \rho_2$, and therefore the breaking of the six-fold rotational symmetry of TBG. Note that this transverse voltage is fundamentally different from the Hall effect since time-reversal symmetry is not broken. In order to quantitatively analyze the transverse voltage, we need to remove any residual longitudinal component that might appear in the transverse voltage due to imperfect alignment of the four-probe voltage contacts and/or sample inhomogeneity (see also Supplementary Materials) *(35)*. Fig. 3A shows the raw R_{xx} and R_{xy} measured for device A near the wedge-like feature, as shown in Fig. 2A. At high temperatures (40 K), where the anisotropies associated with electron correlation effects are presumably overwhelmed by thermal fluctuations, both R_{xx} and R_{xy} are linear in T and proportional to each other: $R_{xy} \approx -0.05R_{xx}$ (*35*). To correct for this background signal that is likely a result of the imperfect voltage probe alignment, we subtract this R_{xx} component from R_{xy} so that at the highest temperature of 40 K the net signal is zero. This corrected transverse voltage $R_{xy}^{cr} = R_{xy} - \alpha(n)R_{xx}$, where $\alpha(n)$ is a density-dependent numerical factor typically within ±0.1, constitutes an accurate measure of the resistivity anisotropy (purple curve in Fig. 3A). We note that, while no signal is present at higher temperatures, below 6 K there is a significant negative peak in R_{xy}^{cr}, which indicates the onset of anisotropy at this temperature.

The gate and temperature dependence of the anisotropy, shown in Figs. 3B and 3C for zero magnetic field and $B_\perp = 0.5$ T (see Supplementary Materials), clearly reveals a prominent anisotropy 'wedge' as well. The transverse voltage measured at $B_\perp = 0.5$ T is symmetrized with data measured at $B_\perp = -0.5$ T to remove the contribution from the Hall voltage. Here we plot the normalized quantity R_{xy}^{cr}/R_{xx}, which is approximately proportional to the anisotropy ratio $(\rho_1 - \rho_2)/(\rho_1 + \rho_2)$ (see Supplementary Materials). We also mark out the superconducting dome in Fig. 3B and 3C. Immediately above the superconducting dome on the 'underdoped' side (lower $|n|$), we find a strong transverse voltage signal with a sign change at around -1.59×10^{12} cm^{-2} (see Supplementary Materials Fig. S2 for the entire range of density). The position of the anisotropy wedge matches well with the resistive wedge-like feature that we observed in Fig. 2A. The sign change indicates that the anisotropy changes from $\rho_1 > \rho_2$ to $\rho_1 < \rho_2$ (or vice versa). In $B_\perp = 0.5$ T (Fig. 3C), the anisotropy wedge with negative values of R_{xy}^{cr} persists to zero temperature, consistent with the behavior of the resistive wedge-like feature in Fig. 2B as well. On the other hand, we notice that the anisotropy with positive R_{xy}^{cr} near -1.65×10^{12} cm^{-2} disappears as superconductivity is suppressed by the magnetic field, which might be explained by the vestigial order from the nematic superconductivity that will be discussed in the next section.

Nematic Superconducting State

A natural question to ask is whether the superconducting phase exhibits any anisotropic properties as well. To investigate this, we measure the angle-dependent in-plane magnetic field response of the superconducting phase. In magic-angle TBG, the superconductivity is suppressed

by an in-plane magnetic field of the same order of magnitude as the Pauli paramagnetic limit (*26*). Using a vector magnet in a dilution refrigerator, we apply a magnetic field $B_{//}$ up to 1 T in an arbitrary direction within the sample plane (see Fig. 4A for illustration). We compensate for possible sample tilt by applying a small out-of-plane magnetic field, so that the magnetic field is parallel to the sample to within $|B_{\perp}| < 2$ Mt at $|B_{//}| = 1$ T, which is much less than the perpendicular critical magnetic field of our devices (see Supplementary Materials and Fig. S3 for detailed calibration procedure, and see Fig. S5 for the perpendicular critical magnetic field of devices A and B). Figure 4B shows an example of the resistivity versus in-plane magnetic field magnitude $|B_{//}|$ and angle θ_B (with respect to the length of the Hall bar, see Fig. 4A). A two-fold anisotropic suppression of the superconductivity can be clearly seen. We have checked that the direction of the current flow is not correlated with the anisotropy direction, and therefore the anisotropic Lorentz force contribution can be excluded (see Supplementary Materials Fig. S6). The anisotropy is not aligned with the length or width of the Hall bar either (see Supplementary Materials Fig. S6).

The two-fold anisotropy of the in-plane magnetotransport response points towards nematicity that is intrinsic to the superconducting phase, since it breaks the six-fold rotational symmetry of the moiré superlattice. We have systematically studied this nematic behavior across the entire superconducting dome of device B. In Figs. 4E to 4R we show polar maps of the magneto-resistivity at different carrier densities and temperatures in the hole-doping and electron-doping superconducting domes as labeled in Fig. 4C. At all densities except those in Figs. 4N and 4R, we find elliptic contours that have major/minor axis ratio up to ~3. Note that we chose to always measure near T_c, since deep inside the superconducting dome the in-plane critical field is usually larger than 1 T and cannot be measured in our setup. However, we have confirmed the nematicity in the $T \ll T_c$ region by simultaneously applying a small perpendicular field to partially suppress the superconducting state (see Supplementary Materials Fig. S7). At the densities corresponding to Figs. 4N and 4R, which are outside the superconducting regions, the anisotropy is essentially nonexistent. In general, the two-fold anisotropy occurs inside the broad transition from superconducting to normal state as a function of $B_{//}$, suggesting that it is a property intrinsic of the superconducting fluctuations *(37)*, since the normal state does not show any anisotropy in the in-plane magnetoresistance (see Fig. S9). In device A, we have also observed similar two-fold anisotropic in-plane critical field (Fig. 4D). The critical magnetic field $B_{c,//}$ along the major axis extrapolated to zero temperature exceeds that along the minor axis by 40~80% in this device.

Figure 4S shows the evolution of the magnitude and of the director of the nematic component of the superconducting state in device B as a function of carrier density and temperature. Our data shows that the nematic director, as measured by the angle of rotation of the ellipse's major axis, does not appear to be exactly locked to any particular spatial axis, but instead evolves continuously with carrier density and temperature. In particular, in the superconducting dome on the hole-doping side of $-n_s/2$, the direction of the major axis varies slowly within -10~+20° in the density range of $-1.70\times10^{12} \sim -1.45\times10^{12}$ cm^{-2} (corresponding to the ellipses from Figs. 4E to 4H), while in the range of $-1.45\times10^{12} \sim -1.25\times10^{12}$ cm^{-2} (from Figs. 4I to 4M) the major axis rotates quickly with the carrier density. From Figs. 4i to 4m, the major axis rotates by ~90°. We note that the latter range of density again coincides with the resistive wedge-like feature for device B, as shown from Figs. 2B and 2D. The smaller superconducting dome on the electron-doping side near -1.20×10^{12} cm^{-2} exhibits significant nematicity as well (Figs. 4P and 4Q), with a director pointing from 120° to 160°. As we explain below, the fact that the nematic director

changes direction as a function of doping and temperature makes it unlikely that the superconducting anisotropy is simply a response to strain present in the sample. On the contrary, this observation is consistent with spontaneous rotational symmetry-breaking characteristic of an intrinsic nematic superconductor.

Anisotropic Response of the Superconducting Gap

The observation of nematicity puts certain constraints on possible pairing symmetries of the superconducting order parameter (*14*, *38*, *39*). One can obtain information about the superconducting gap by measuring the critical current I_c. Here, by measuring I_c of device B in the presence of in-plane magnetic fields, we demonstrate that the nematicity is not only manifested in the resistivity measurements, but also creates an anisotropic modulation of the superconducting gap. Figures 5A-B show the waterfall plots of differential resistance dV_{xx}/dI_{bias} versus dc bias current I_{bias} at two carrier densities, in an in-plane magnetic field $|B_{//}| = 1$ T along different directions indicated by the colors. At the carrier density in Fig. 5B, the plot shows two critical currents at 110 nA and 210 nA respectively, which might be due to domains in the device with different twist angles or nematic directors. Interestingly, at both carrier densities the critical current shows significant two-fold modulation by the in-plane magnetic field direction θ_B. The θ_B-dependence can be fit by a sinusoidal function $\cos2(\theta_B-\theta_{B0})$ (Fig. 5C), where θ_{B0} is the direction of the major axis. The modulation amplitude as a function of the in-plane field magnitude is shown in the inset of Fig. 5C, and follows an approximately quadratic power law dependence.

An anisotropic response in the critical current may originate from (i) the superconducting gap Δ and/or (ii) anisotropic properties of the underlying normal state resistance (R_n). Although we have shown that the normal state exhibits considerable resistivity anisotropy at densities near the wedge-like feature in Fig. 3, we argue here that the anisotropic response of the critical current is not a result of the anisotropy of R_n. First, Fig. 5A is measured at a density for which there is essentially no resistivity anisotropy in the normal state ($R_{xy}^{cr}/R_{xx} = -0.007$ at the lowest T in Fig. 3C), while Fig. 5B is measured at one with significant anisotropy in the normal state (R_{xy}^{cr}/R_{xx} $/R_{xx} = -0.325$ at the lowest T in Fig. 3C). However, the modulation of the critical current at these two densities shows similar magnitudes. Second, an anisotropy in the resistivity tensor may not necessarily imply a large anisotropic response of the resistivity versus in-plane magnetic field. In fact, as we show in the Supplementary Material Fig. S9, inside the wedge-like feature in the normal state in device A, we could not measure significant anisotropic response to the in-plane field. Thus, these results suggest that the anisotropic response of the critical current might not be directly related to the resistivity anisotropy of the normal state and hence may originate from an anisotropic superconducting gap.

To discuss the mechanism by which the in-plane field couples to the superconducting gap, we note that if the former couples solely to the spin degree of freedom (and thus the gap is only suppressed by the Zeeman coupling), spin-orbit interaction must be introduced to explain the dependence of I_c on the direction of $B_{//}$. However, the intrinsic spin-orbit coupling in graphene-based systems is known to be very weak. We might consider the following mechanism to reconcile these facts. As illustrated in Fig. 1A, the unit cell of magic-angle TBG has a length scale of a~14 nm. Despite the separation between the graphene sheets in TBG being merely δ~0.3 nm, an in-plane magnetic field penetrating them induces a small but non-negligible

magnetic flux in the cross-section of the unit cell with an area $S \sim a\delta$, which modifies the Fermi contours. To demonstrate this effect, we numerically calculated the Fermi contours at $-n_s/2$ for $B_{//} = 0$ and $B_{//} = 1$ T along the x direction using the Bistritzer-MacDonald continuum model (*28*). Figs. 5D and 5E show the original and modified Fermi contours for the K and K' valleys respectively. As can be seen from the contours, a noticeable shift is induced by the in-plane magnetic field. The K/K' valley degeneracy is lifted by the momentum shift between the two layers introduced by the in-plane field, which is proportional to $e\delta B_{//}$, a substantial shift given the small size of the Brillouin zone. If one assumes that only electrons with opposite momentum and valley are allowed to form Cooper pairs in the superconducting phase, the two states from opposite valleys would be at slightly different energies when an in-plane field is applied, which serves to suppress the superconductivity in a similar fashion as the paramagnetic (Zeeman) effect in the case of spins. To more intuitively demonstrate this, Fig. 5F shows the de-pairing energy along the Fermi contour $\Delta E(\boldsymbol{k}) = E_{K'}(\boldsymbol{k}) - E_K(-\boldsymbol{k})$. It is strongly directional dependent and has a similar order of magnitude as the Zeeman energy at $B_{//}$=1 T ($g\mu_B B_{//} \approx 115$ μeV, where $g = 2$, μ_B is the Bohr magneton). The de-pairing energy exhibits a six-fold variation with respect to the direction of the in-plane magnetic field, while the nematic component of the superconducting order can further spontanously break this symmetry down to the observed two-fold symmetry (*37*, *38*, *40*). A small strain can further assist to pin down the nematic domain along a given direction.

Discussion

Our measurements reveal two distinct anisotropic states in the phase diagram of magic-angle TBG: a normal-state wedge-like feature above the superconducting dome and a nematic pairing state. As shown by the longitudinal resistivity and transverse voltage measurements presented in Fig. 2 and Fig. 3, the wedge-like feature is associated with a zero-temperature insulating phase that shows significant resistivity anisotropy, indicative of broken six-fold lattice rotational symmetry. Thus, this normal state phase might be either an electronic nematic state or an electronic smectic state — i.e. a charge or spin density-wave that, in addition to rotational symmetry, also breaks translational lattice symmetry. In either case, the rotational symmetry-breaking can be described by a two-component 3-state Potts nematic order parameter **(*40*, *41*)**. Electronic correlations might be important for the formation of such a state. Twisted bilayer graphene is well-known to exhibit van Hove singularities (vHs), which in general do not occur exactly at half-filling **(*42*, *43*)**. Near the vHs, it has been theoretically shown that the significant nesting between the K- and K'-valley Fermi contours might induce density wave ordering (*39*). Remarkably, recent scanning tunneling experiments have identified prominent rotational-symmetry-broken features in the normal state local density of states **(*44*–*46*)**. Alternatively, strong-coupling models can also yield nematic and density-wave states **(*47*, *48*)**. For the superconducting phase, it remains to be seen whether its nematic character, as revealed by the measured in-plane anisotropy of the critical field, can be reconciled with s-wave pairing. Alternatively, this behavior could be explained in terms of a two-component p-wave/d-wave gap, indicative of an unconventional pairing mechanism **(*49*)**.

A crucial question is whether the anisotropies observed here have intrinsic or extrinsic origins. The fact that we do not observe multiple nematic domains within the same device implies that some degree of residual strain is present. The issue is whether this strain is the sole cause of the anisotropy (extrinsic origin), or whether it is mainly pinning one of the three underlying nematic

domains (intrinsic origin). To address this, we note that such a residual strain should be a property of the device, and thus should be present at all temperatures and doping. In contrast, as shown in Fig. 3, the onset of the normal-state anisotropy is restricted to a narrow doping range and to temperatures below 10 K. Furthermore, the resistance anisotropy is on the order of one in the 'wedge'-like feature (see Fig. 3B). Such a large effect would be difficult to be explained by a reasonably sized residual strain.

While these quantitative arguments rely on the amplitude of the anisotropy, a more direct argument against an extrinsic origin can be made from the direction of the anisotropy. Our measurements in the superconducting state clearly show a rotation of the nematic director (Figs. 4E to 4R, and 4S). In the 3-state Potts model, the three states correspond to the three nearest-neighbor directions in the moiré superlattice **(*40*)**. Here, strain acts as a conjugate field to the nematic order parameter, similarly to how a magnetic field acts on a ferromagnet. If the strain is 'parallel' to one of the three anisotropy directions, the corresponding nematic director is favored over the other two. As a result, the nematic director is fixed at all temperatures. If the strain is 'anti-parallel' to a direction, the other two directions become favored. Consequently, as the temperature is lowered towards the nematic state, the nematic director continuously rotates from the disfavored direction to one of the two favored directions **(*40*)**. Importantly, this can only happen if nematic order is spontaneous, *i.e.* if it is an intrinsic instability of the system, as it is supported by a phenomenological calculation shown in the Supplementary Material. Therefore, the continuous rotation of the nematic director in our observation indicates that the anisotropy of the superconducting state is more likely to be intrinsic, as an extrinsic origin would result in a fixed orientation.

Another possible source of anisotropy is twist angle variations across the device, which could create an inhomogeneous distribution of strain **(*50*)**. While further studies are needed, we note that such an inhomogeneous strain would act as a random field to the Potts-nematic order parameter, which might affect the nematic properties in 2D **(*51*)**. However, the fact that we do not see different nematic domains across our device seems to suggest that the global residual strain is probably dominating over the local strain caused by twist angle fluctuations.

The various phases discussed throughout this article are summarized in Fig. 6 (see Supplementary Materials and Fig. S8 for the extracted nematicity temperature T_{nem}). The fact that an anisotropic response to an in-plane magnetic field is seen only in the superconducting state, but not in the wedge-like feature, suggests that the origins of nematicity in the normal and superconducting states are likely different. This is also consistent with the fact that these two orders compete, as evident from the suppression of T_c when the wedge-like feature intersects with the superconducting dome. However, since both phases break the same six-fold lattice rotational symmetry, the order parameters of these two phases can interact beyond mere competition, which may be responsible for the rapid change of the ellipse direction in the coexisting region of the phase diagram (see Supplementary Material). Moreover, normal-state nematic fluctuations may play an important role in favoring a superconducting ground state that is also nematic. While the onset of nematicity and of superconductivity seem very close in our experiment (see Supplementary Material), it is possible that the nematic order in magic-angle TBG persists even above T_c, a phenomenon known as vestigial nematic order **(*12*, *14*, *41*)**. Interestingly, in Fig. 3B, there is a region just above the superconducting dome with positive transverse voltage signal at $n \approx -1.65\times10^{12}$ cm^{-2} and $T \approx 2$ K. This not only has opposite sign than the anisotropy of the wedge-like state, but it also disappears when superconductivity is

suppressed (Fig. 3C). Thus, this feature might be explained by a vestigial nematic order that forms prior to the condensation of Cooper pairs (***12***, ***14***, ***41***). Scanning probe experiments are encouraged in the future to confirm this nematic phase above the superconducting transition.

In summary, our experiments extend the already rich phase diagram of magic-angle TBG to include a nematic superconducting state and an anisotropic normal state above the 'underdoped' part of the superconducting dome. The competition between them results in a reduction of T_c and in a fast rotation of the nematic director of the superconducting state. Our results pioneer the study of competing/intertwined quantum phases in a highly tunable two-dimensional correlated platform, which in turn may shed more light onto the unconventional superconductivity in iron-based compounds, doped Bi_2Se_3 and other nematic superconductors.

References and Notes:

1. P. W. Anderson, More Is Different. *Science*. **177**, 393–396 (1972).

2. S. Sachdev, Colloquium: Order and quantum phase transitions in the cuprate superconductors. *Rev. Mod. Phys.* **75**, 913–932 (2003).

3. B. Keimer, S. A. Kivelson, M. R. Norman, S. Uchida, J. Zaanen, From quantum matter to high-temperature superconductivity in copper oxides. *Nature*. **518**, 179–186 (2015).

4. E. Fradkin, S. A. Kivelson, M. J. Lawler, J. P. Eisenstein, A. P. Mackenzie, Nematic Fermi Fluids in Condensed Matter Physics. *Annual Review of Condensed Matter Physics*. **1**, 153–178 (2010).

5. R. M. Fernandes, A. V. Chubukov, J. Schmalian, What drives nematic order in iron-based superconductors? *Nature Physics*. **10**, 97–104 (2014).

6. V. Hinkov, D. Haug, B. Fauqué, P. Bourges, Y. Sidis, A. Ivanov, C. Bernhard, C. T. Lin, B. Keimer, Electronic Liquid Crystal State in the High-Temperature Superconductor YBa2Cu3O6.45. *Science*. **319**, 597–600 (2008).

7. J.-H. Chu, H.-H. Kuo, J. G. Analytis, I. R. Fisher, Divergent Nematic Susceptibility in an Iron Arsenide Superconductor. *Science*. **337**, 710–712 (2012).

8. T.-M. Chuang, M. P. Allan, J. Lee, Y. Xie, N. Ni, S. L. Bud'ko, G. S. Boebinger, P. C. Canfield, J. C. Davis, Nematic Electronic Structure in the "Parent" State of the Iron-Based Superconductor Ca(Fe1–xCox)2As2. *Science*. **327**, 181–184 (2010).

9. E. P. Rosenthal, E. F. Andrade, C. J. Arguello, R. M. Fernandes, L. Y. Xing, X. C. Wang, C. Q. Jin, A. J. Millis, A. N. Pasupathy, Visualization of electron nematicity and unidirectional antiferroic fluctuations at high temperatures in NaFeAs. *Nature Physics*. **10**, 225–232 (2014).

10. B. E. Feldman, M. T. Randeria, A. Gyenis, F. Wu, H. Ji, R. J. Cava, A. H. MacDonald, A. Yazdani, Observation of a nematic quantum Hall liquid on the surface of bismuth. *Science*. **354**, 316–321 (2016).

11. Y. Sato, S. Kasahara, H. Murayama, Y. Kasahara, E.-G. Moon, T. Nishizaki, T. Loew, J. Porras, B. Keimer, T. Shibauchi, Y. Matsuda, Thermodynamic evidence for a nematic phase transition at the onset of the pseudogap in YBa 2 Cu 3 O y. *Nature Physics*. **13**, 1074–1078 (2017).

12. L. Nie, G. Tarjus, S. A. Kivelson, Quenched disorder and vestigial nematicity in the pseudogap regime of the cuprates. *Proceedings of the National Academy of Sciences*. **111**, 7980–7985 (2014).

13. E. Fradkin, S. A. Kivelson, J. M. Tranquada, Colloquium: Theory of intertwined orders in high temperature superconductors. *Rev. Mod. Phys.* **87**, 457–482 (2015).

14. R. M. Fernandes, P. P. Orth, J. Schmalian, Intertwined Vestigial Order in Quantum Materials: Nematicity and Beyond. *Annual Review of Condensed Matter Physics*. **10**, 133–154 (2019).

15. C. Proust, L. Taillefer, The Remarkable Underlying Ground States of Cuprate Superconductors. *Annu. Rev. Condens. Matter Phys.* **10**, 409–429 (2019).

16. J. Chang, E. Blackburn, A. T. Holmes, N. B. Christensen, J. Larsen, J. Mesot, R. Liang, D. A. Bonn, W. N. Hardy, A. Watenphul, M. v Zimmermann, E. M. Forgan, S. M. Hayden, Direct observation of competition between superconductivity and charge density wave order in YBa 2 Cu 3 O 6.67. *Nature Physics*. **8**, 871–876 (2012).

17. S. D. Edkins, A. Kostin, K. Fujita, A. P. Mackenzie, H. Eisaki, S. Uchida, S. Sachdev, M. J. Lawler, E.-A. Kim, J. C. S. Davis, M. H. Hamidian, Magnetic field–induced pair density wave state in the cuprate vortex halo. *Science*. **364**, 976–980 (2019).

18. J. Li, P. J. Pereira, J. Yuan, Y.-Y. Lv, M.-P. Jiang, D. Lu, Z.-Q. Lin, Y.-J. Liu, J.-F. Wang, L. Li, X. Ke, G. Van Tendeloo, M.-Y. Li, H.-L. Feng, T. Hatano, H.-B. Wang, P.-H. Wu, K. Yamaura, E. Takayama-Muromachi, J. Vanacken, L. F. Chibotaru, V. V. Moshchalkov, Nematic superconducting state in iron pnictide superconductors. *Nature Communications*. **8**, 1880 (2017).

19. J. Shen, W.-Y. He, N. F. Q. Yuan, Z. Huang, C. Cho, S. H. Lee, Y. S. Hor, K. T. Law, R. Lortz, Nematic topological superconducting phase in Nb-doped Bi 2 Se 3. *npj Quantum Materials*. **2**, 1–7 (2017).

20. A. Y. Kuntsevich, M. A. Bryzgalov, V. A. Prudkoglyad, V. P. Martovitskii, Y. G. Selivanov, E. G. Chizhevskii, Structural distortion behind the nematic superconductivity in $Sr_x Bi_2 Se_3$. *New J. Phys.* **20**, 103022 (2018).

21. K. Matano, M. Kriener, K. Segawa, Y. Ando, G. Zheng, Spin-rotation symmetry breaking in the superconducting state of Cu x Bi 2 Se 3. *Nature Physics*. **12**, 852–854 (2016).

22. T. Asaba, B. J. Lawson, C. Tinsman, L. Chen, P. Corbae, G. Li, Y. Qiu, Y. S. Hor, L. Fu, L. Li, Rotational Symmetry Breaking in a Trigonal Superconductor Nb-doped Bi2Se3. *Phys. Rev. X*. **7**, 011009 (2017).

23. Y. Pan, A. M. Nikitin, G. K. Araizi, Y. K. Huang, Y. Matsushita, T. Naka, A. de Visser, Rotational symmetry breaking in the topological superconductor Sr x Bi 2 Se 3 probed by upper-critical field experiments. *Scientific Reports*. **6**, 28632 (2016).

24. M. P. Smylie, K. Willa, H. Claus, A. E. Koshelev, K. W. Song, W.-K. Kwok, Z. Islam, G. D. Gu, J. A. Schneeloch, R. D. Zhong, U. Welp, Superconducting and normal-state anisotropy of the doped topological insulator Sr 0.1 Bi 2 Se 3. *Scientific Reports*. **8**, 7666 (2018).

25. Y. Cao, V. Fatemi, A. Demir, S. Fang, S. L. Tomarken, J. Y. Luo, J. D. Sanchez-Yamagishi, K. Watanabe, T. Taniguchi, E. Kaxiras, R. C. Ashoori, P. Jarillo-Herrero, Correlated insulator behaviour at half-filling in magic-angle graphene superlattices. *Nature*. **556**, 80–84 (2018).

26. Y. Cao, V. Fatemi, S. Fang, K. Watanabe, T. Taniguchi, E. Kaxiras, P. Jarillo-Herrero, Unconventional superconductivity in magic-angle graphene superlattices. *Nature*. **556**, 43–50 (2018).

27. E. Suárez Morell, J. D. Correa, P. Vargas, M. Pacheco, Z. Barticevic, Flat bands in slightly twisted bilayer graphene: Tight-binding calculations. *Phys. Rev. B*. **82**, 121407 (2010).

28. R. Bistritzer, A. H. MacDonald, Moiré bands in twisted double-layer graphene. *PNAS*. **108**, 12233–12237 (2011).

29. J. M. B. Lopes dos Santos, N. M. R. Peres, A. H. Castro Neto, Continuum model of the twisted graphene bilayer. *Phys. Rev. B*. **86**, 155449 (2012).

30. M. Yankowitz, S. Chen, H. Polshyn, Y. Zhang, K. Watanabe, T. Taniguchi, D. Graf, A. F. Young, C. R. Dean, Tuning superconductivity in twisted bilayer graphene. *Science*. **363**, 1059–1064 (2019).

31. Y. Cao, J. Y. Luo, V. Fatemi, S. Fang, J. D. Sanchez-Yamagishi, K. Watanabe, T. Taniguchi, E. Kaxiras, P. Jarillo-Herrero, Superlattice-Induced Insulating States and Valley-Protected Orbits in Twisted Bilayer Graphene. *Phys. Rev. Lett.* **117**, 116804 (2016).

32. K. Kim, M. Yankowitz, B. Fallahazad, S. Kang, H. C. P. Movva, S. Huang, S. Larentis, C. M. Corbet, T. Taniguchi, K. Watanabe, S. K. Banerjee, B. J. LeRoy, E. Tutuc, van der Waals Heterostructures with High Accuracy Rotational Alignment. *Nano Lett.* **16**, 1989–1995 (2016).

33. X. Lu, P. Stepanov, W. Yang, M. Xie, M. A. Aamir, I. Das, C. Urgell, K. Watanabe, T. Taniguchi, G. Zhang, A. Bachtold, A. H. MacDonald, D. K. Efetov, Superconductors, orbital magnets and correlated states in magic-angle bilayer graphene. *Nature*. **574**, 653–657 (2019).

34. B. J. Ramshaw, S. E. Sebastian, R. D. McDonald, J. Day, B. S. Tan, Z. Zhu, J. B. Betts, R. Liang, D. A. Bonn, W. N. Hardy, N. Harrison, Quasiparticle mass enhancement approaching optimal doping in a high-Tc superconductor. *Science*. **348**, 317–320 (2015).

35. P. Walmsley, I. R. Fisher, Determination of the resistivity anisotropy of orthorhombic materials via transverse resistivity measurements. *Review of Scientific Instruments*. **88**, 043901 (2017).

36. J. Wu, A. T. Bollinger, X. He, I. Božović, Spontaneous breaking of rotational symmetry in copper oxide superconductors. *Nature*. **547**, 432–435 (2017).

37. J. W. F. Venderbos, V. Kozii, L. Fu, Identification of nematic superconductivity from the upper critical field. *Phys. Rev. B*. **94**, 094522 (2016).

38. V. Kozii, H. Isobe, J. W. F. Venderbos, L. Fu, Nematic superconductivity stabilized by density wave fluctuations: Possible application to twisted bilayer graphene. *Phys. Rev. B*. **99**, 144507 (2019).

39. H. Isobe, N. F. Q. Yuan, L. Fu, Unconventional Superconductivity and Density Waves in Twisted Bilayer Graphene. *Phys. Rev. X*. **8**, 041041 (2018).

40. R. M. Fernandes, J. W. F. Venderbos, Nematicity with a twist: Rotational symmetry breaking in a moiré superlattice. *Science Advances*. **6**, eaba8834 (2020).

41. M. Hecker, J. Schmalian, Vestigial nematic order and superconductivity in the doped topological insulator Cu x Bi 2 Se 3. *npj Quantum Materials*. **3**, 1–6 (2018).

42. G. Li, A. Luican, J. M. B. Lopes dos Santos, A. H. Castro Neto, A. Reina, J. Kong, E. Y. Andrei, Observation of Van Hove singularities in twisted graphene layers. *Nat. Phys.* **6**, 109–113 (2010).

43. A. Luican, G. Li, A. Reina, J. Kong, R. R. Nair, K. S. Novoselov, A. K. Geim, E. Y. Andrei, Single-Layer Behavior and Its Breakdown in Twisted Graphene Layers. *Phys. Rev. Lett.* **106**, 126802 (2011).

44. A. Kerelsky, L. J. McGilly, D. M. Kennes, L. Xian, M. Yankowitz, S. Chen, K. Watanabe, T. Taniguchi, J. Hone, C. Dean, A. Rubio, A. N. Pasupathy, Maximized electron interactions at the magic angle in twisted bilayer graphene. *Nature*. **572**, 95–100 (2019).

45. Y. Jiang, X. Lai, K. Watanabe, T. Taniguchi, K. Haule, J. Mao, E. Y. Andrei, Charge order and broken rotational symmetry in magic-angle twisted bilayer graphene. *Nature*. **573**, 91–95 (2019).

46. S.-Y. Li, K.-Q. Liu, L.-J. Yin, W.-X. Wang, W. Yan, X.-Q. Yang, J.-K. Yang, H. Liu, H. Jiang, L. He, Splitting of Van Hove singularities in slightly twisted bilayer graphene. *Phys. Rev. B*. **96**, 155416 (2017).

47. J. Kang, O. Vafek, Strong Coupling Phases of Partially Filled Twisted Bilayer Graphene Narrow Bands. *Phys. Rev. Lett.* **122**, 246401 (2019).

48. J. F. Dodaro, S. A. Kivelson, Y. Schattner, X. Q. Sun, C. Wang, Phases of a phenomenological model of twisted bilayer graphene. *Phys. Rev. B*. **98**, 075154 (2018).

49. D. V. Chichinadze, L. Classen, A. V. Chubukov, Valley magnetism, nematicity, and density wave orders in twisted bilayer graphene. *Phys. Rev. B*. **102**, 125120 (2020).

50. A. Uri, S. Grover, Y. Cao, J. A. Crosse, K. Bagani, D. Rodan-Legrain, Y. Myasoedov, K. Watanabe, T. Taniguchi, P. Moon, M. Koshino, P. Jarillo-Herrero, E. Zeldov, Mapping the twist-angle disorder and Landau levels in magic-angle graphene. *Nature*. **581**, 47–52 (2020).

51. D. Blankschtein, Y. Shapir, A. Aharony, Potts models in random fields. *Phys. Rev. B*. **29**, 1263–1267 (1984).

52. K. Kim, A. DaSilva, S. Huang, B. Fallahazad, S. Larentis, T. Taniguchi, K. Watanabe, B. J. LeRoy, A. H. MacDonald, E. Tutuc, Tunable moiré bands and strong correlations in small-twist-angle bilayer graphene. *PNAS*. **114**, 3364–3369 (2017).

53. L. Wang, I. Meric, P. Y. Huang, Q. Gao, Y. Gao, H. Tran, T. Taniguchi, K. Watanabe, L. M. Campos, D. A. Muller, J. Guo, P. Kim, J. Hone, K. L. Shepard, C. R. Dean, One-Dimensional Electrical Contact to a Two-Dimensional Material. *Science*. **342**, 614–617 (2013).

54. L. Zou, H. C. Po, A. Vishwanath, T. Senthil, Band structure of twisted bilayer graphene: Emergent symmetries, commensurate approximants, and Wannier obstructions. *Phys. Rev. B*. **98**, 085435 (2018).

55. M. Koshino, N. F. Q. Yuan, T. Koretsune, M. Ochi, K. Kuroki, L. Fu, Maximally Localized Wannier Orbitals and the Extended Hubbard Model for Twisted Bilayer Graphene. *Phys. Rev. X*. **8**, 031087 (2018).

56. S. Liu, E. Khalaf, J. Y. Lee, A. Vishwanath, Nematic topological semimetal and insulator in magic angle bilayer graphene at charge neutrality. *arXiv:1905.07409 [cond-mat]* (2020) (available at http://arxiv.org/abs/1905.07409).

57. R. M. Fernandes, A. J. Millis, Nematicity as a Probe of Superconducting Pairing in Iron-Based Superconductors. *Phys. Rev. Lett.* **111**, 127001 (2013).

58. Y. Saito, J. Ge, K. Watanabe, T. Taniguchi, A. F. Young, Independent superconductors and correlated insulators in twisted bilayer graphene. *Nature Physics*, 1–5 (2020).

59. M. Sigrist, K. Ueda, Phenomenological theory of unconventional superconductivity. *Rev. Mod. Phys.* **63**, 239–311 (1991).

Acknowledgments: We acknowledge helpful discussions with P. A. Lee, S. Todadri, A. Vishwanath, A. Hristov, I. Fisher, J. Venderbos, and S. A. Kivelson; **Funding:** This work has been supported by the STC Center for Integrated Quantum Materials (NSF Grant No. DMR-1231319) for most devices' fabrication, transport measurements, and data analysis (Y.C., D.R.-L., P.J.-H.). J.M.P. acknowledges the US Department of Energy (DOE), Office of Basic Energy

Sciences (BES), Division of Materials Sciences and Engineering under Award DE-SC0001819 for additional device fabrication. D.R.-L. acknowledges partial support from Fundación Bancaria 'la Caixa' (LCF/BQ/AN15/10380011) and from the US Army Research Office grant no. W911NF-17-S-0001. P.J-H acknowledges support from the Gordon and Betty Moore Foundation's EPiQS Initiative through Grant GBMF9643. The development of new nanofabrication and characterization techniques enabling this work has been supported by the US DOE Office of Science, BES, under award DE-SC0019300. K.W. and T.T. acknowledge support from the Elemental Strategy Initiative conducted by the MEXT, Japan, Grant Number JPMXP0112101001, JSPS KAKENHI Grant Numbers JP20H00354 and the CREST(JPMJCR15F3), JST. This work made use of the Materials Research Science and Engineering Center Shared Experimental Facilities supported by the National Science Foundation (DMR-0819762) and of Harvard's Center for Nanoscale Systems, supported by the NSF (ECS-0335765). R.M.F. (phenomenological modeling) acknowledges support by the U. S. Department of Energy, Office of Science, Basic Energy Sciences, Materials Sciences and Engineering Division, under Award No. DE-SC0020045. N.F.Q.Y. and L.F. (in-plane field modeling) were supported by the US DOE, Office of Science, Office of Basic Energy Sciences (BES), Division of Materials Sciences and Engineering under Award DE-SC0018945; **Author contributions:** Y.C., D.R.-L. and J.M.P. fabricated samples and performed transport measurements. Y.C., D.R.-L., and P.J-H. performed data analysis and discussed the results. P.J-H supervised the project. N.F.Q.Y., L.F., and R.M.F. provided theoretical support. K.W. and T.T. provided h-BN samples. Y.C., D.R.-L. and P.J.-H. co-wrote the manuscript with input from all co-authors; **Competing interests:** The authors declare no competing financial interest; and **Data and materials availability:** The data presented in this work can be requested from the corresponding authors upon reasonable request.

Supplementary Materials:

Materials and Methods

Figures S1-S12

Tables S1

References **(*52*–*59*)**

Fig. 1. Characterization and statistics of magic-angle twisted bilayer graphene (TBG) devices. (A) Illustration of the moiré pattern in magic-angle TBG. The color scale shows the normalized local density in the flat bands when the twist angle is close to magic angle. The twist angle of the displayed pattern is enlarged for clarity. (B) Resistivity of device A (twist angle $\theta = 1.09°$) versus gate induced carrier density and temperature, showing correlated features at all integer electron fillings of the superlattice. Superconductivity is found at hole-doping of the $-n_s/2$ insulator with critical temperature ~2.5 K. (C) Resistivity versus temperature for devices A and B, with twist angles $\theta = 1.09°$ and $\theta = 1.08°$, respectively, at their optimal doping concentrations. Inset shows the forward and backward sweeps of the *V*-*I* curves in device B which exhibit a significant hysteresis. (D) Temperature dependence of the *V*-*I* curves measured in device B. Inset shows the log-log plot of the $I > 0$ part of the data. The Berezinskii-Kosterlitz-Thouless transition temperature $T_{BKT} \approx 2.2$ K is identified where the slope of the curve crosses $d(\log V_{xx})/d(\log I) = 3$ (equivalent to $V_{xx} \propto I^3$). (E) Statistics of optimal doping T_c in 14 of the magic-angle TBG devices we have measured. We find that the trend of T_c peaks around 1.1°, the theoretically predicted

first magic-angle in TBG. The green data points are from devices exhibiting substantial disorder, hence the large error bars in the twist angle determination. This disorder may be responsible for the relatively low T_c. The orange and purple bars denote the range of twist angles where we have observed anisotropic normal state and nematic superconductivity, respectively. The latter has been seen in all the devices where it was investigated (see Table S1 in Supplementary Materials), and hence we have added dashed purple lines to the edge of the purple line to indicate that those devices might likely also exhibit nematic superconductivity.

Fig. 2. Competing phases near the superconducting domes of magic-angle TBG. (A-B) Resistivity versus gate-induced carrier density and temperature for device A and device B, respectively. (C-D) Same measurement but in a perpendicular magnetic field of 0.5 T. (E-F) Line cuts of resistivity versus temperature for devices A and B at 0 T and 0.5 T at the densities indicated by the dashed lines in (A-D), showing a superconductor-to-insulator transition induced by the magnetic field. In both devices, we find a wedge-like feature above the superconducting dome in addition to the $-n_s/2$ correlated state. This feature shifts noticeably towards negative relative densities at elevated temperatures. At zero magnetic field, the wedge-like feature disappears into the superconducting dome and creates a 'kink' on the $T_c(n)$ curve, while in 0.5 T it persists down to the lowest temperatures and turns into an insulator. The gray circles in (A-D) indicate the resistivity maxima associated with the wedge-like feature at different temperatures. (G) Evolution of T_c of device A in a perpendicular magnetic field up to 0.18 T. Each contour line is T_c (10% normal resistance) versus carrier density at the magnetic field indicated by the color shading. The yellow band represents the approximate position of the wedge-like feature. At $B_\perp =$ 0.09 T (orange curve), the T_c-kink touches zero at the same density where the wedge-like feature extrapolates to zero temperature. Above this field, the superconducting dome splits into two domes roughly centered at -1.52×10^{12} cm^{-2} and -1.67×10^{12} cm^{-2}, respectively.

Fig. 3. Normal-state anisotropy in magic-angle TBG device A. (A) Illustration of how we extract the resistivity anisotropy by measuring the transverse resistance. Inset shows the actual device configuration that we used to obtain the data, where black arrows indicate current source and drain. R_{xx}, R_{xy} label the leads on which longitudinal and transverse resistances are measured, respectively. The purple trace, R_{xy}^{cr}, is the transverse resistance corrected for leads misalignment (see Supplementary Materials). $n = -1.53\times10^{12}$ cm^{-2} in this measurement. (B-C) Anisotropy ratio versus carrier density and temperature at zero magnetic field and $B_\perp = 0.5$ T, respectively (see Supplementary Materials). The circles in (B) and the dashed line in (C) outline the approximate shape of the superconducting dome (at zero field). We find the strongest anisotropy near the kink in T_c at $n = -1.54\times10^{12}$ cm^{-2}, coinciding with the resistive wedge-like feature we identified in Fig. 2A and 2G.

Fig. 4. Evidence for nematic superconductivity in magic-angle TBG. (A) Definition of the in-plane field angle θ_B with respect to the device orientation. $\theta_B = 0$ (x-axis) is defined as the source-drain direction of the Hall bar device. (B) Resistivity as a function of θ_B for different magnitudes of the in-plane magnetic field, showing a clear two-fold anisotropy. Measurement is taken at $n =$ -1.18×10^{12} cm^{-2} and $T = 70$ mK. (C) Detailed view of the superconducting domes in device B, showing a large and a small superconducting dome on the p-side and n-side of the insulating state. (D) Critical in-plane magnetic field $B_{c,//}$ versus temperature along the major and minor axis of the two-fold anisotropy, measured in device A at carrier densities of -1.44×10^{12} cm^{-2}, -1.42×10^{12} cm^{-2}, -1.40×10^{12} cm^{-2} and -1.23×10^{12} cm^{-2} respectively (from right to left). (E-R) Polar

maps of the anisotropic response of the resistivity across the superconducting domes in device B. The carrier densities and temperatures at which (E-R) are measured correlate with the labels in (C). (S) For device B, we extracted the magnitude (represented by height) and the polar angle of the major axis θ_{maj} (represented by the color, see Supplementary Materials for details) of the nematicity at different densities and temperatures, with $|B_{//}| = 1$ T. The data for different temperatures are shifted vertically for clarity. Inside the region shaded in purple, the critical in-plane magnetic field is larger than 1 T and cannot be measured in our setup. In the density range of $-1.45\times10^{12} \sim -1.2\times10^{12}$ cm^{-2}, the anisotropy polar angle θ_{maj} rotates rapidly with the carrier density, possibly due to the competition with the wedge-like feature we identified in Fig. 2 and Fig. 3.

Fig. 5. Anisotropic response of the superconducting critical current. (A-B) Differential resistance dV_{xx}/dI_{bias} versus bias current I_{bias} as a function of the orientation of the in-plane magnetic field at two carrier densities. The orientation is indicated by the color, differing by 15° between adjacent curves, which are vertically shifted for clarity. (C) Modulation of the larger critical current in (B) by in-plane magnetic fields with different orientations and magnitudes. A sinusoidal function is used to fit the data (see main text). The inset shows the modulation amplitude (peak-peak) as a function of the field magnitude, which can be fit by a power law $\Delta I_c \propto |B_{//}|^{\alpha}$ with $\alpha \approx 2.1$. (D-E) Calculated Fermi contour of $\theta = 1.09°$ TBG at $B_x = 0$ and $B_x = 1$ T around K and K' valleys respectively. (F) Energy splitting between states at opposite momentum and opposite valleys along the Fermi surface $\Delta E(\boldsymbol{k}) = E_{K'}(\boldsymbol{k}) - E_K(-\boldsymbol{k})$ at $B_x = 1$ T. For comparison, the Zeeman splitting $g\mu_B B$ at $B = 1$ T for $g = 2$ is 115 μeV. The gray hexagons in (D-F) denote the moiré Brillouin zone.

Fig. 6. Summary of various competing phases we identified in this article. In the underdoped side of the superconducting dome, we find a normal state anisotropic phase that, at low temperatures, competes with superconductivity, creating a depression in the T_c curve. In the superconducting state we find nematicity, manifested in its response to in-plane magnetic fields. By comparing the extracted nematicity temperature T_{nem} to T_c we find that the entire superconducting dome exhibits nematicity, which suggests that the nematicity is intrinsic to the superconductivity and points towards a possible unconventional pairing symmetry. The dashed area denotes the competing region between the two states, where a reduction in T_c as well as a strong rotation of the nematicity axis are seen.

Figure 1

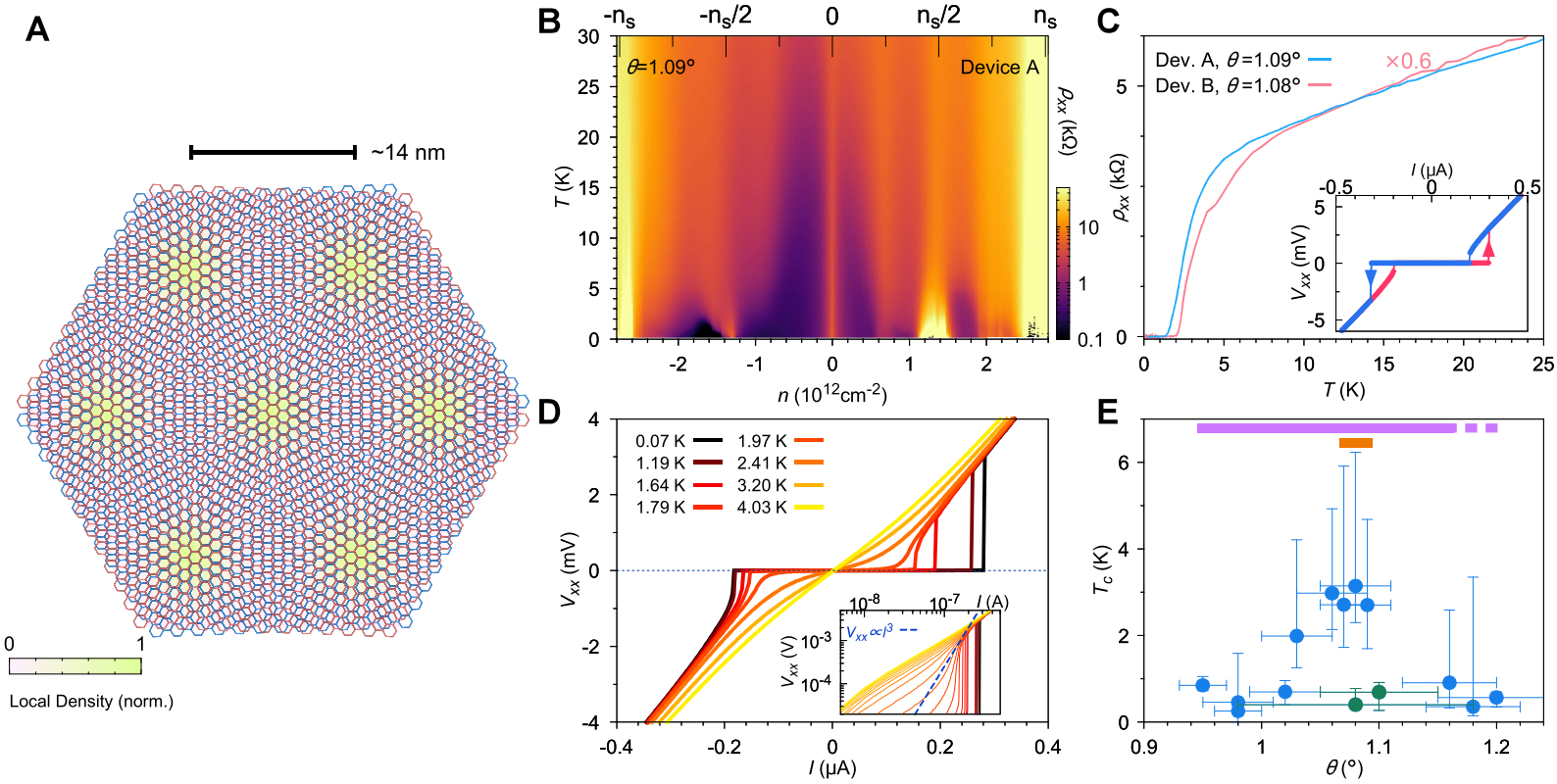
A
~14 nm
0
1
Local Density (norm.)
B
-n_s
-n_s/2
0
n_s/2
n_s
θ=1.09°
Device A
T (K)
n (10^12 cm^-2)
ρ_xx (kΩ)
C
Dev. A, θ=1.09°
Dev. B, θ=1.08°
×0.6
ρ_xx (kΩ)
T (K)
I (μA)
V_xx (mV)
D
0.07 K
1.19 K
1.64 K
1.79 K
1.97 K
2.41 K
3.20 K
4.03 K
V_xx (mV)
I (μA)
V_xx ∝ I^3
V_xx (V)
I (A)
E
T_c (K)
θ (°)

Figure 2

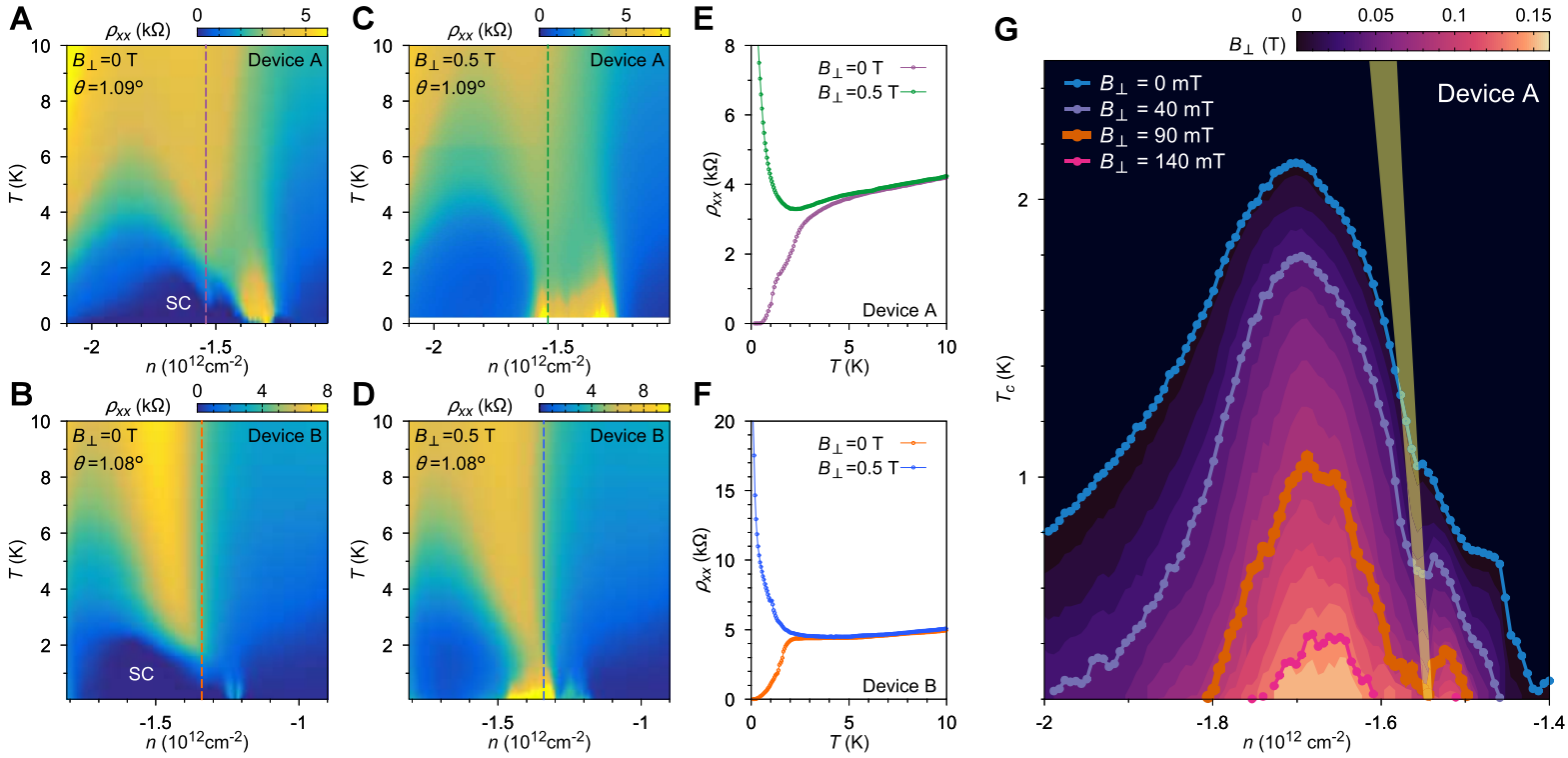
A
B
C
D
E
F
G
ρ_{xx} (kΩ)
$B_\perp$=0 T
θ=1.09°
θ=1.08°
$B_\perp$=0.5 T
Device A
Device B
SC
T (K)
n (10^{12}cm^{-2})
$B_\perp$ = 0 mT
$B_\perp$ = 40 mT
$B_\perp$ = 90 mT
$B_\perp$ = 140 mT
$B_\perp$ (T)
T_c (K)

Figure 3

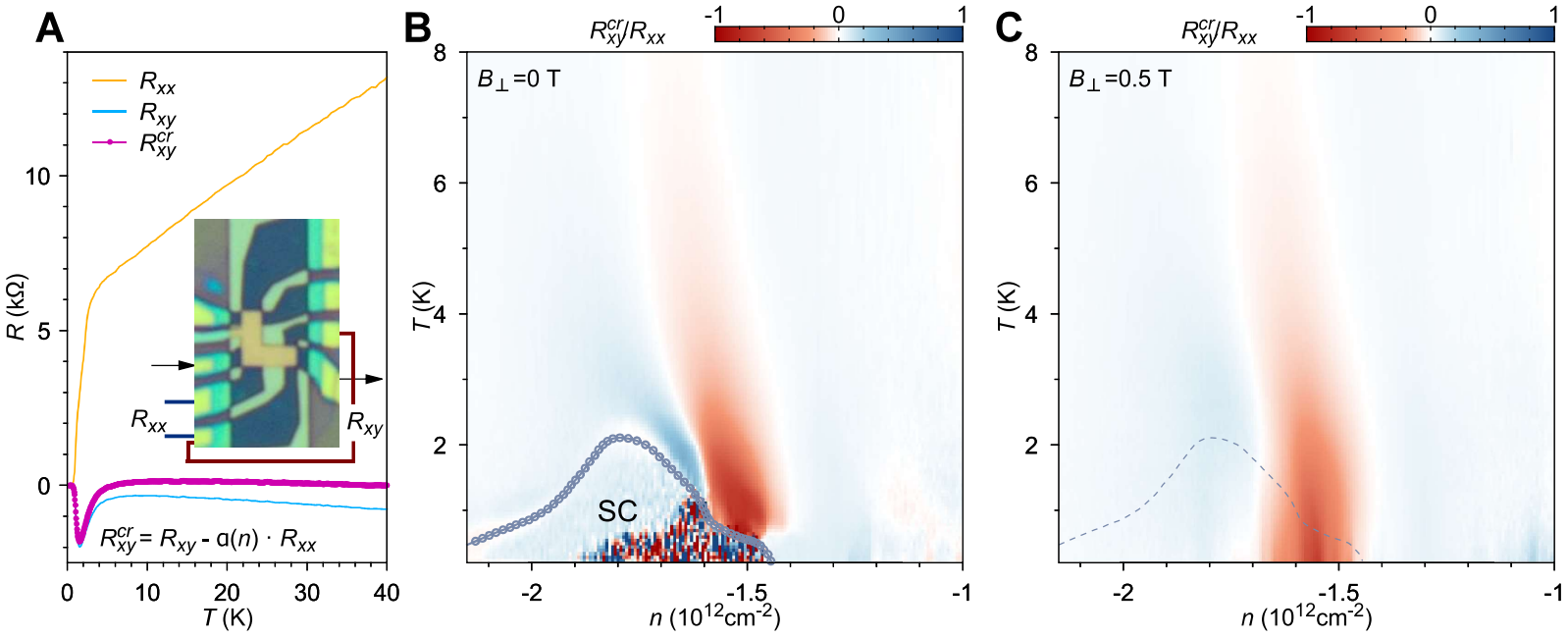
A
B
C
R_{xx}
R_{xy}
R^{cr}_{xy}
R^{cr}_{xy} = R_{xy} - α(n) · R_{xx}
R (kΩ)
T (K)
R^{cr}_{xy}/R_{xx}
$B_\perp$=0 T
$B_\perp$=0.5 T
SC
n (10^{12}cm^{-2})

Figure 4

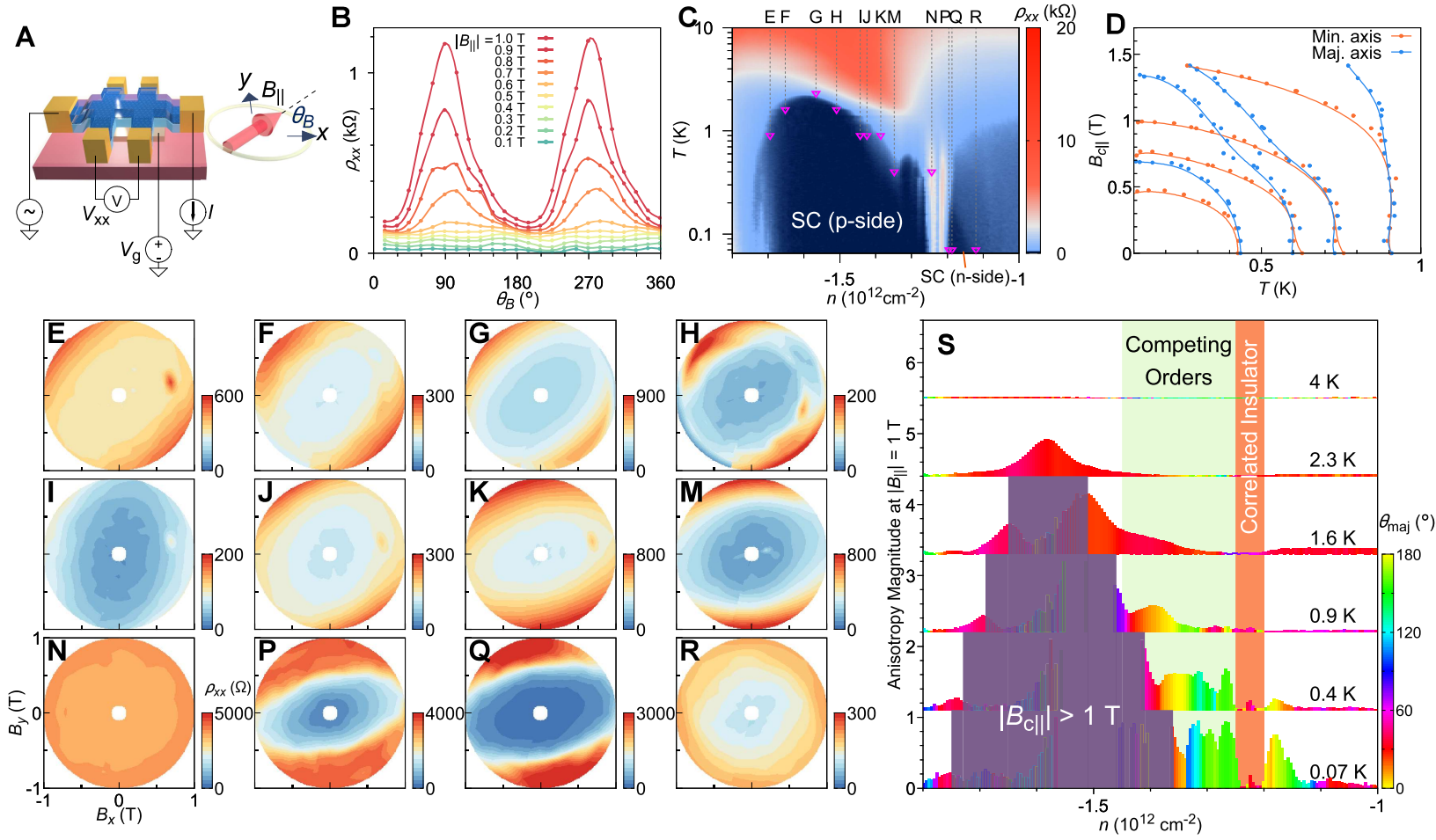
A
B
C
D
E
F
G
H
I
J
K
M
N
P
Q
R
S
SC (p-side)
SC (n-side)
Min. axis
Maj. axis
Competing Orders
Correlated Insulator
4 K
2.3 K
1.6 K
0.9 K
0.4 K
0.07 K
|Bc||| > 1 T

Figure 5

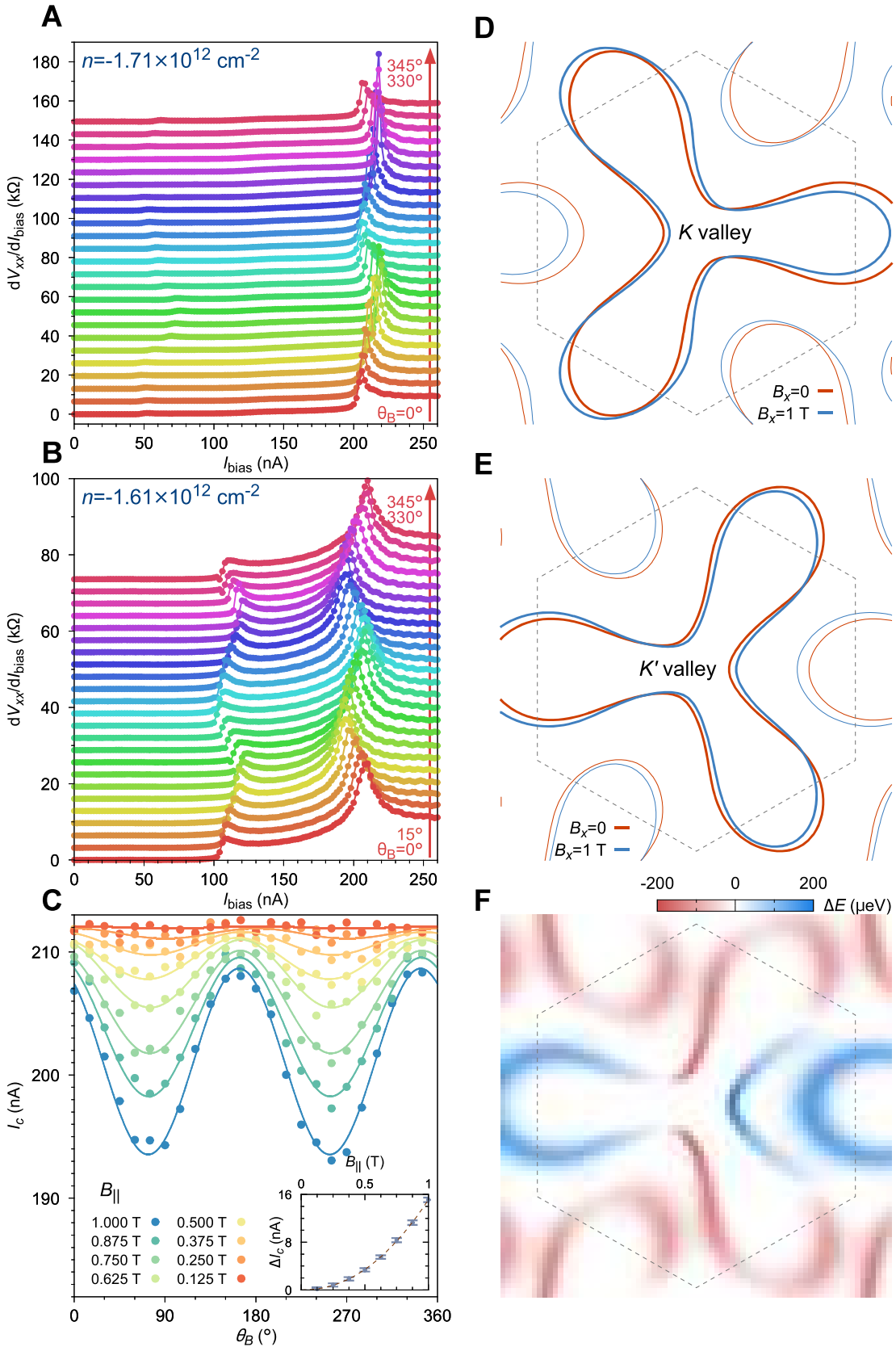
A
n=-1.71×10^12 cm^-2
345°
330°
θB=0°
dVxx/dIbias (kΩ)
Ibias (nA)
B
n=-1.61×10^12 cm^-2
345°
330°
15°
θB=0°
dVxx/dIbias (kΩ)
Ibias (nA)
C
Ic (nA)
B|| (T)
B||
1.000 T
0.875 T
0.750 T
0.625 T
0.500 T
0.375 T
0.250 T
0.125 T
ΔIc (nA)
θB (°)
D
K valley
Bx=0
Bx=1 T
E
K′ valley
Bx=0
Bx=1 T
-200
0
200
ΔE (μeV)
F

Figure 6

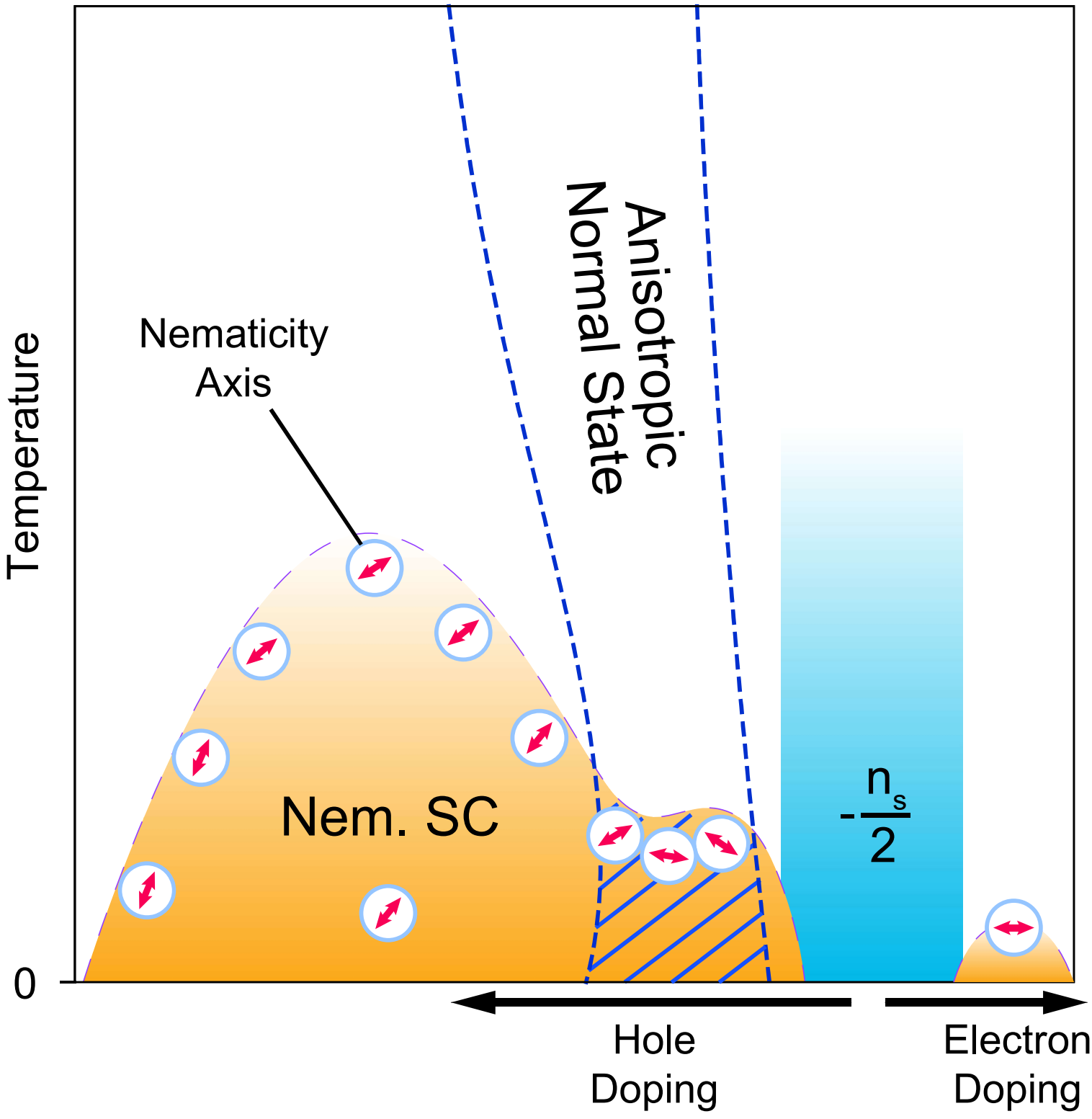
Temperature
0
Nematicity
Axis
Anisotropic
Normal State
Nem. SC
$-\frac{n_s}{2}$
Hole
Doping
Electron
Doping

Supplementary Material of "Nematicity and Competing Orders in Superconducting Magic-Angle Graphene"

Contents

1 Sample Fabrication

We fabricate high quality magic-angle twisted bilayer graphene (TBG) devices using a previously developed 'tear & stack' technique, detailed in [32] and Refs. [31, 52]. Specifically, monolayer graphene and hexagonal boron nitride (h-BN, $\sim 50\,\mathrm{nm}$ thick) are exfoliated on SiO_2/Si substrated, annealed at $350\,^{\circ}\mathrm{C}$ (only for h-BN) and examined using optical microscopy and atomic force microscopy. A PC/PDMS polymer stack on a glass slide mounted on a micropositioning stage is used to pick up a h-BN flake. Then we use the van der Waals force between h-BN and graphene to tear a graphene flake. The substrate is rotated by $\theta \approx 1.2^{\circ}$, and the other piece of graphene is then picked up, creating the desired TBG structure. The resulting stack is encapsulated with another h-BN flake of similar thickness, and put onto a Cr/PdAu gate evaporated and lift-off on another SiO_2/Si substrate. The device geometry is defined by electron-beam lithography and reactive ion etching, which only leaves behind regions free of any bubbles or wrinkles. Electrical connections to the TBG are made by one-dimensional edge contacts [53].

2 Measurement Setup and Data Analysis

We perform transport measurements using low-frequency lock-in amplifiers with excitation frequency between $2\,\mathrm{Hz}$ to $10\,\mathrm{Hz}$ and excitation current $I_{\mathrm{ac}} \approx 1\,\mathrm{nA}$. The sample resistance is obtained by dividing the four-probe voltage V_{xx} by the current flowing through the sample I, independently measured by two lock-in amplifiers. For transverse voltage measurements, a third lock-in is used to measure V_{xy}.

The twist angles of the devices are determined from the magnetotransport data (the Landau fan diagram). The details are described in the Methods section of our previous works [25, 26]. The error bars in Fig. 1E are estimated by visually inspecting how well the Landau levels emanating from the Dirac point, $\pm n_s/2$ and $\pm n_s$ fit to the expected Landau fan of a given twist angle.

3 Additional Data and Discussion

3.1 Landau Fan Diagram

To demonstrate the high quality and similarity in device A and device B that we discussed throughout the manuscript, in Fig. S1 we show the Landau fan diagram of device A measured at low temperatures. The Landau fan diagram of device B can be found in Fig. 1 of Ref. [50], which is measured on the same device. Note that in Ref. [50], the twist angle is determined to be $\theta = 1.06^{\circ}$, while in this work we assign a value of $\theta = (1.08 \pm 0.03)^{\circ}$. In both devices A and B, we observe 4-fold degenerate Landau levels at the charge neutrality, which break down to two-fold or one-fold at high fields. We also observe two-fold degenerate levels emanating from $\pm n_s/2$, consistent with the original report in magic-angle TBG [26].

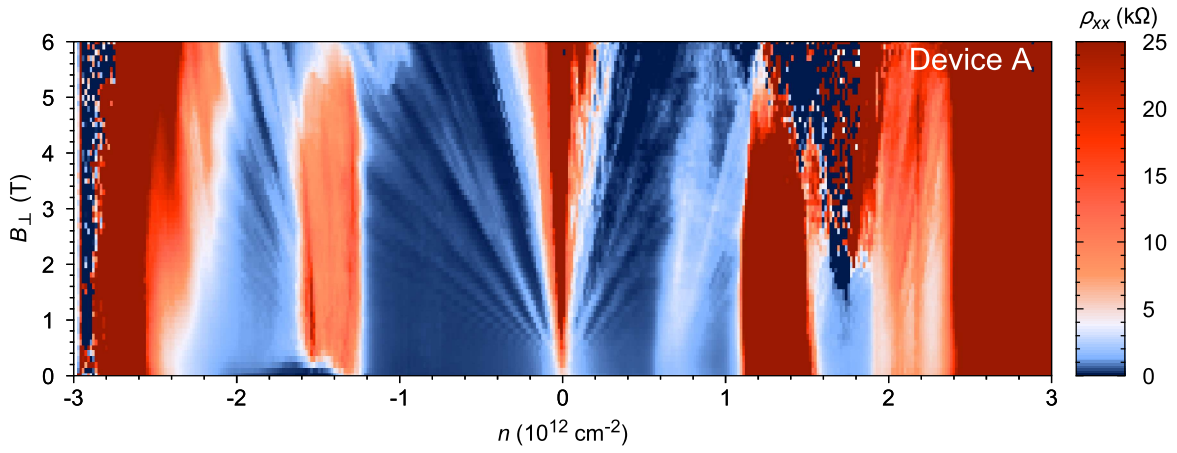

Figure S1: Landau fan diagram of device A, measured at the base temperature $T = 70\,\mathrm{mK}$.

3.2 Normal-state anisotropy measured through transverse voltage

In Fig. 3 we use transverse voltage measurements to infer possible anisotropy in the resistivity tensor when $T > T_c$. Specifically, an anisotropic 2D conductor has different resistivity along its principle axis

$$\rho = \begin{pmatrix} \rho_1 & 0 \\ 0 & \rho_2 \end{pmatrix}, \tag{1}$$

where $\rho_1 \neq \rho_2$. In a reference frame that is rotated from the principle axis by θ, the resistivity tensor transforms as

$$\rho' = \begin{pmatrix} \frac{1}{2}(\rho_1+\rho_2) + \frac{1}{2}(\rho_1-\rho_2)\cos(2\theta) & \frac{1}{2}(\rho_1-\rho_2)\sin(2\theta) \\ \frac{1}{2}(\rho_1-\rho_2)\sin(2\theta) & \frac{1}{2}(\rho_1+\rho_2) - \frac{1}{2}(\rho_1-\rho_2)\cos(2\theta) \end{pmatrix} \tag{2}$$

Therefore, the off-diagonal term $\rho'_{12} = \rho'_{21}$ is proportional to the anisotropy in resistivity $\rho_1 - \rho_2$. This term can be experimentally observed in the transverse voltage configuration by measuring $R_{xy} = V_y/I_x$, similar to Hall effect measurement except that no external magnetic field is applied. In actual devices, however, R_{xy} is frequently measured to be non-zero even in isotropic materials due to R_{xx} mix-in. This can for example occur due to imperfect alignment of the transverse voltage probes, obscuring the anisotropic signal by introducing a large background [35]. The mix-in results in a component in R_{xy} that is proportional to R_{xx} at all temperatures. To account for this, we assume that the device is isotropic at high temperatures, so that ρ_{12} is zero, and then estimate the contribution from the R_{xx} mix-in by dividing the measured R_{xy} over R_{xx} at this temperature for each density n, obtaining the ratio $\alpha(n) = R_{xy}(T_{\max})/R_{xx}(T_{\max})$. Assuming the mix-in is temperature independent, we subtract the contribution proportional to R_{xx} at all temperatures. This corrected R_{xy} is denoted as $R^{\mathrm{cr}}_{xy}(n,T) = R_{xy}(n,T) - \alpha(n)R_{xx}(n,T)$, which by definition satisfies $R^{\mathrm{cr}}_{xy}(T = T_{\max}) = 0$. Finally, we normalize the corrected quantity

by R_{xx}, which is approximately related to the anisotropy as

$$\frac{R_{xy}^{\mathrm{cr}}}{R_{xx}} \approx \frac{W}{L}\frac{\rho_1-\rho_2}{\rho_1+\rho_2}\sin(2\theta) \approx \frac{W}{L}\frac{\Delta\rho}{2\rho}\sin(2\theta), \tag{3}$$

provided that $\rho_1 - \rho_2 \ll \rho_1, \rho_2$. L and W are the length and width of the sample respectively. Unless the device is coincidentally aligned with the anisotropy axis such that $\theta = 0$, this normalized quantity is characteristic of the anisotropy ratio $\frac{\Delta\rho}{\rho}$. It should be noted that this measurement always tends to *underestimate* the anisotropy, since $|\sin(2\theta)| < 1$.

In a perpendicular magnetic field, the transverse voltage will attain an additional Hall component proportional to $B_\perp$. To probe the normal-state anisotropy in a small perpendicular magnetic field, we measure R_{xy} at both $B_\perp$ and $-B_\perp$ and take the average between them. The R_{xy} signal symmetrized in this fashion would in principle contain no Hall voltage and is attributed only to the anisotropy.

In addition to the vicinity of the superconducting domes, we measured the transverse voltage in the entire flat-band densities $-n_s \leq n \leq n_s$, up to $40\,\mathrm{K}$. As shown in Fig. S1, we find that there is considerable anisotropy near $+n_s/2$ and $+3n_s/4$ as well, which might be related to the same type of phase that is responsible for the anisotropy near $-n_s/2$. Noticeably, near the Dirac point ($n = 0$) there is a diffuse triangular region with weak anisotropy that changes direction as n crosses zero. This phenomena might be related to the recently proposed nematic topological semimetallic behavior near the charge neutrality point of TBG. [56] Recent scanning tunneling experiments also show evidence of C_3-symmetry breaking near the charge neutrality of magic-angle TBG [45].

3.3 Compensation for device tilt in in-plane magnetic field measurements

The in-plane field behavior of the TBG devices is measured in an American Magnetics Inc. 3-axis vector magnet with maximum x/y fields of $1\,\mathrm{T}$. When loading samples into the cryostat, however, it is hardly possible to perfectly align the sample plane to the x-y field plane. Typically the sample is tilted by about 1° to 2° with respect to the field plane.

To calibrate and compensate for this tilt, we use the superconductivity of magic-angle TBG itself to act as a perpendicular magnetic field sensor. Near the edge of the superconducting dome (where superconductivity barely survives), the resistance of the device is highly sensitive to the variation in perpendicular magnetic field and therefore can be used as a reference to nullify the residual perpendicular magnetic field, accurate to $1\,\mathrm{mT}$ to $2\,\mathrm{mT}$. Figure S2a shows examples of resistance versus $B_\perp$ curves at various (B_x, B_y). Sharp reductions of the resistance can be seen in each curve, the center of which we identify as the 'true' zero magnetic field at each (B_x, B_y) point.

We use a two-step procedure to calibrate the sample tilt:

1. Global rough calibration. We measure the perpendicular magnetic field $B_\perp$ at which the resistance is minimized, at a number of points (B_x, B_y), and fit the loci of the minima to

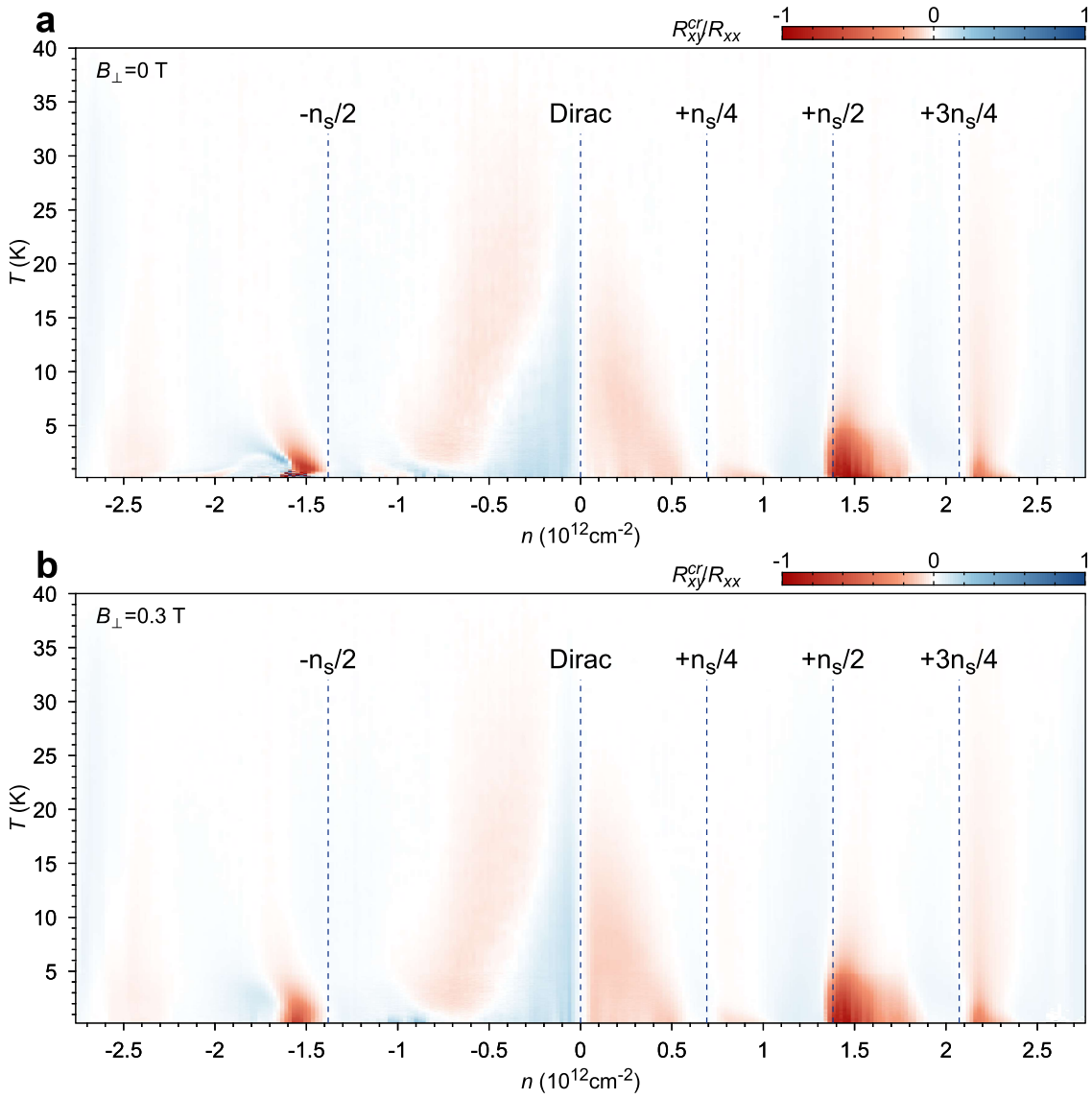

Figure S2: Normal-state anisotropy via transverse voltage measurements in device A. (a) $R_{xy}^{\mathrm{cr}}/R_{xx}$ ratio in device A across the entire density range $-n_s \leq n \leq n_s$ at zero magnetic field. (b) Same measurement, performed at $B_\perp = 0.3\,\mathrm{T}$.

a function in the form of $B_\perp = aB_x + bB_y + c$, to obtain the tilted plane of the sample. Figure S2(b) shows an example of such a plane fit, with an adjusted R^2 of 0.9884 and maximal deviation of $6.6\,\mathrm{mT}$ from the data.

2. Fine calibration. Using the plane-fit value obtained from the global calibration, random

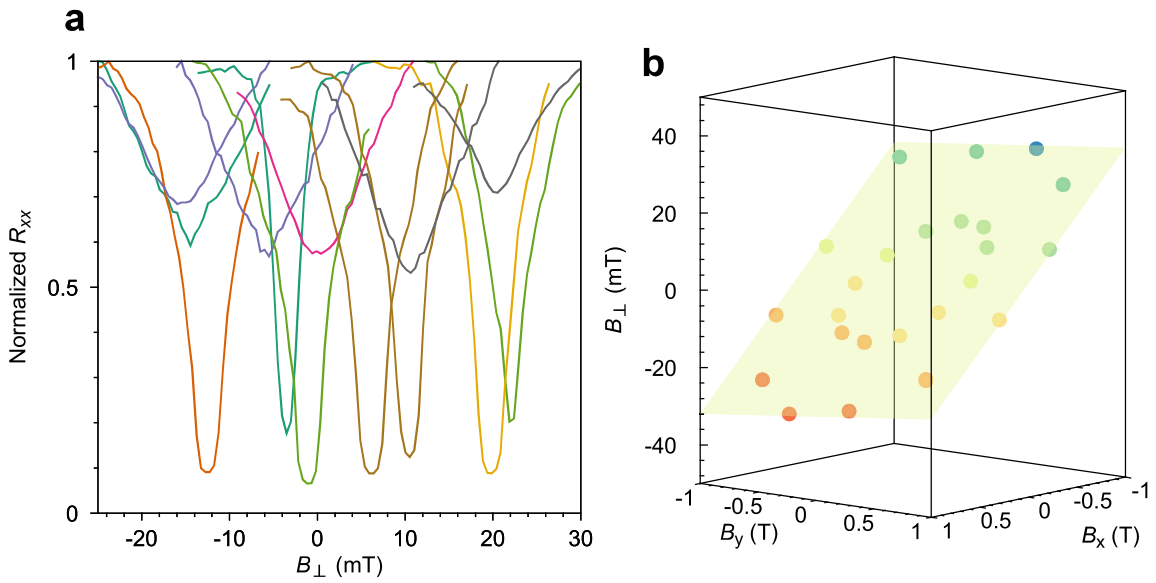

Figure S3: (a) Example curves of normalized R_{xx} used for calibrating offset in perpendicular magnetic field taken at various in-plane fields and temperatures. (b) Example of planar fitting that we use to globally correct for the sample tilt. In this example 24 points are taken in the $B_x - B_y$ plane, and for each point a calibration similar to those shown in (a) is performed and the minimum is plotted in the graph. The plane shown in the graph is a least-square fit of the minima to a plane, $aB_x + bB_y + c$. The coefficients are fit to be $a = -0.029\,99, b = 0.003\,625, c = 0.001\,658\,\mathrm{T}$, with an adjusted R^2 of 0.9884. These values correspond to a tilt angle of about 1.7° from the $B_x - B_y$ plane.

Device	Twist Angle	T_c (50 %)	Anisotropy/Comments
M1	$(1.16 \pm 0.04)^\circ$	0.91 K	SC
M2	$(1.03 \pm 0.03)^\circ$	1.99 K	SC
M3	$(1.10 \pm 0.05)^\circ$	0.69 K	Disordered
M4	$(1.06 \pm 0.03)^\circ$	2.98 K	
M6 (Device B)	$(1.08 \pm 0.03)^\circ$	3.14 K	SC, Normal
M7 (Device A)	$(1.09 \pm 0.02)^\circ$	2.70 K	SC, Normal
M8	$(1.08 \pm 0.10)^\circ$	0.40 K	Disordered
M9	$(1.18 \pm 0.04)^\circ$	0.35 K	
M10	$(0.98 \pm 0.03)^\circ$	0.46 K	
M12	$(0.95 \pm 0.02)^\circ$	0.85 K	SC
M13	$(1.20 \pm 0.05)^\circ$	0.57 K	
M15	$(0.98 \pm 0.02)^\circ$	0.26 K	
M16	$(1.02 \pm 0.03)^\circ$	0.70 K	
M18 (Device C)	$(1.07 \pm 0.02)^\circ$	2.71 K	SC, Normal

Table S1: List of superconducting magic-angle TBG devices.

deviations by more than $5\,\mathrm{mT}$ from the 'true' zero field value still occur, either due to a change in magnetization of the cryostat or tilting/tipping of the sample holder due to magnetic forces. Therefore we perform an additional fine correction around the plane-fit value, whenever B_x or B_y is changed. The principle is the similar: we take a fine scan of $B_\perp$ around the plane-fit value and find the minimum in R_{xx}. This procedure greatly reduces the residual field to $< 2\,\mathrm{mT}$ at the cost of increased measurement time. Any *systematic* error from the sample tilt is in principle eliminated in this step.

3.4 Statistics of Superconducting Devices

Table S1 lists the twist angle and T_c (50 % normal resistance) at optimal doping of all superconducting magic-angle TBG devices we have measured. We show the resistance-temperature (R_{xx}-T) curves for all these listed devices at their optimal doping in Fig. S4. T_c is obtained by first fitting the high temperature part of the R_{xx}-T curve to a straight line $AT + B$, then find the temperature where $R_{xx}(T) = 0.5(AT + B)$. In the last column in Table S1, we also list what type of anisotropy (SC and/or normal state) we measured in each device. The relevant anisotropy/nematicity data are presented in Section 4. Among these devices, M3 and M8 have relatively large twist angle disorder and relatively low T_c accordingly. These points are shown in green color in Fig. 1E in the main text.

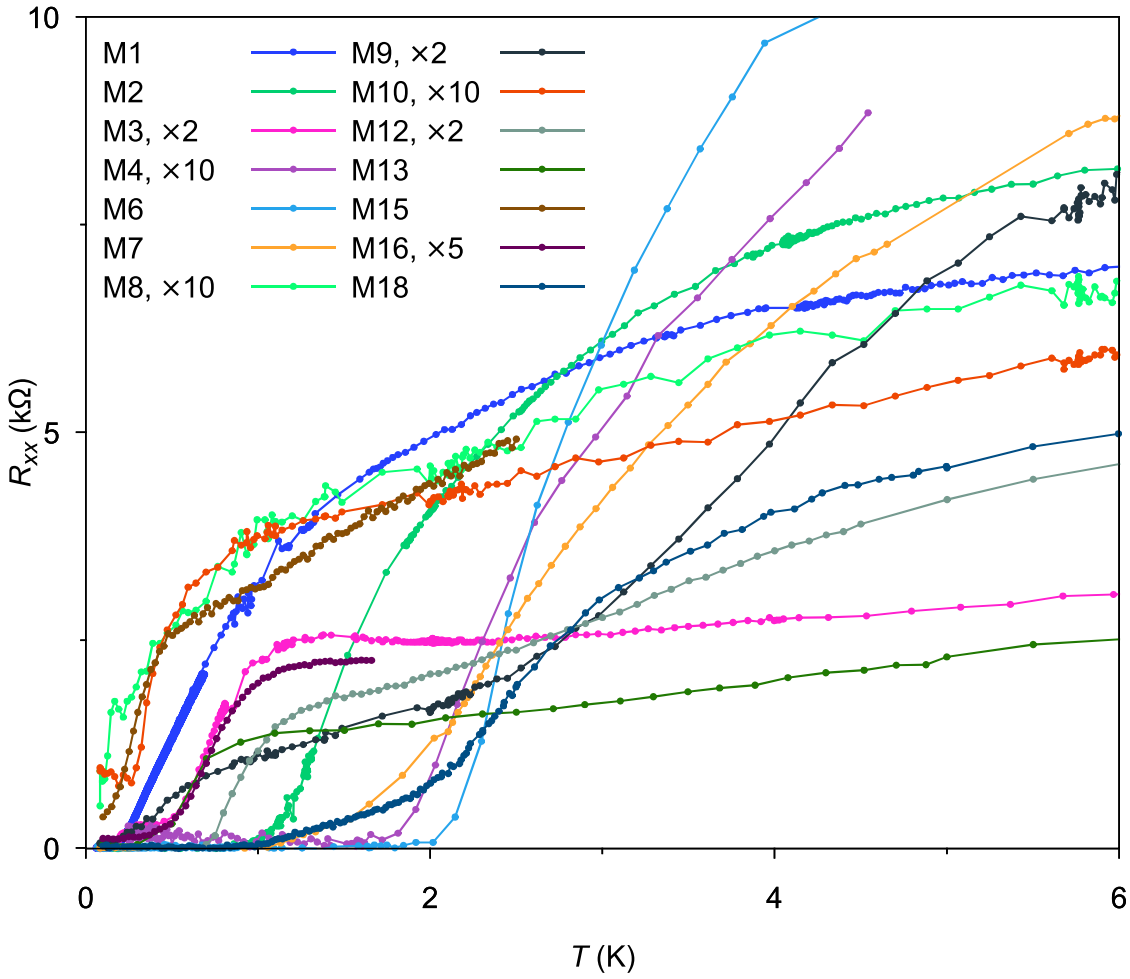

Figure S4: Resistance-temperature curves for the magic-angle TBG devices listed in Table S1.

3.5 Perpendicular Critical Magnetic Field of devices A and B

Figure S5 shows the resistivity ρ_{xx} in device A and B versus carrier density and perpendicular magnetic field $B_\perp$. The maximum critical perpendicular magnetic field of device A is $\sim 0.2\,\mathrm{T}$, and that of device B is $\sim 0.3\,\mathrm{T}$. Therefore, any residual perpendicular field $< 2\,\mathrm{mT}$ that results from imperfect sample tilt correction is much smaller than the critical perpendicular magnetic field and is unlikely to be sufficient to account for the observed two-fold anisotropy.

3.6 Nematicity versus Current Flow Direction

To rule out the possibility that the in-plane field anisotropy is related to the current flow direction (due to Lorentz force acting on the electron movement for example), we measure the anisotropy

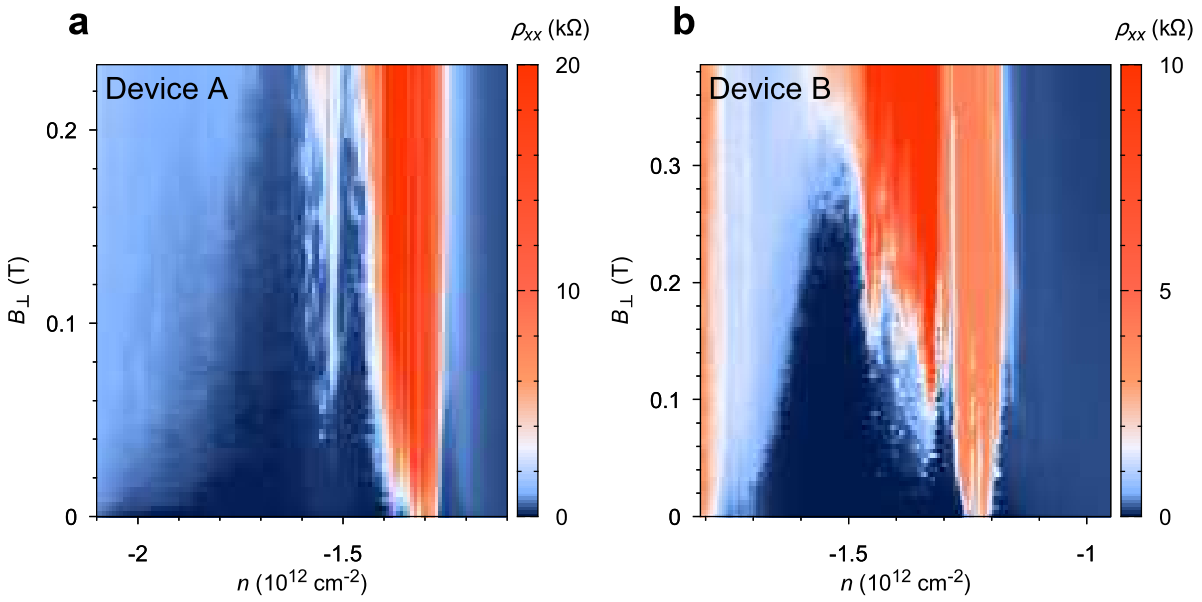

Figure S5: The resistivity ρ_{xx} for (a) device A and (b) device B as functions of carrier density n and perpendicular magneticfield $B_\perp$ respectively. Measurements are performed at $T = 70\,\mathrm{mK}$.

for two perpendicular current flow directions and find that the anisotropy axis is invariant, and not aligned to either of flow directions. We measure the two-probe conductance of the device along x and y directions as illustrated in Fig. S6a and b respectively. The in-plane field magnitude is fixed at $B_\parallel = 1\,\mathrm{T}$ while its orientation is rotated. In both cases, we observe maximum conductance (major axis) along the direction $\theta_B \approx 135°$, which is neither along x ($0°$) nor y ($90°$) axis of the Hall bar. This experiment confirms that the spontaneous symmetry-breaking is intrinsic to TBG instead of being determined by the sample geometry or by the external current.

3.7 Nematicity vs. Temperature and Perpendicular Field

To demonstrate the nematicity across the entire superconducting dome, we have measured the $B_\parallel$-θ_B maps of resistivity across the superconducting dome at six different temperatures, $0.07\,\mathrm{K}$, $0.4\,\mathrm{K}$, $0.9\,\mathrm{K}$, $1.7\,\mathrm{K}$, $2.3\,\mathrm{K}$ and $4\,\mathrm{K}$ respectively. As the temperature is raised, the magnitude of the nematicity in general decreases. We analyze the in-plane magneto-transport data by comparing the resistance measured at $|B_\parallel| = 1\,\mathrm{T}$ along different directions. We extract the anisotropy magnitude, defined as $A = (\rho_{\max} - \rho_{\min})/(\rho_{\max} + \rho_{\min})$, as well as the azimuthal angle of the major axis θ_{maj} along which the resistivity is lowest. These results are summarized in Fig. 4S, with the anisotropy magnitude and the major axis angle represented by the height and the color of the bars respectively, at each of the measured temperatures.

In Fig. 4S, in a range of densities near the optimal doping density, $-1.6 \times 10^{-12}\,\mathrm{cm}^{-2}$, the nematicity cannot be measured because the critical magnetic field is higher than the maximum

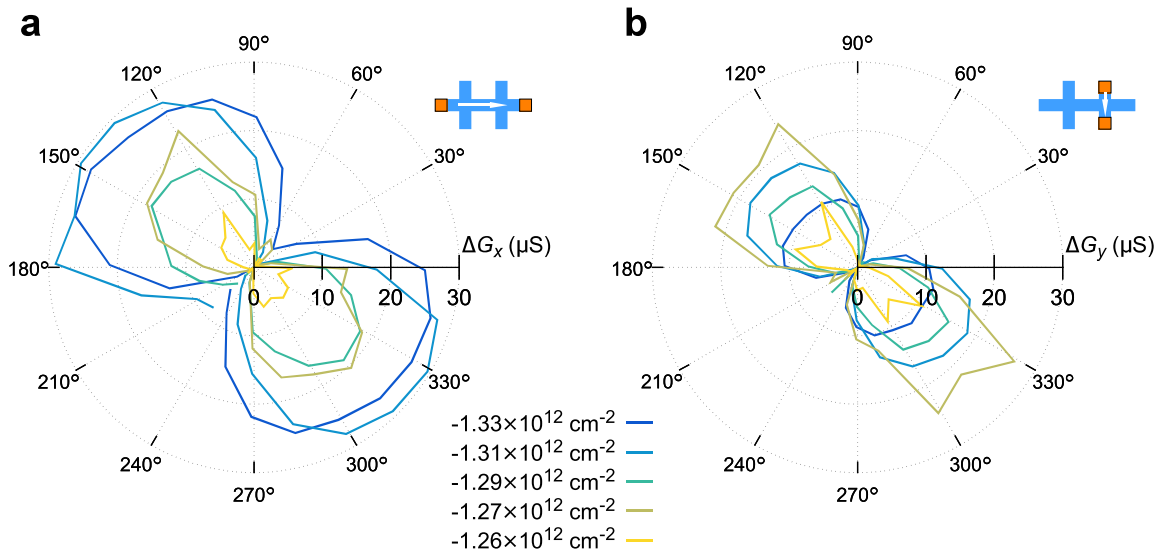

Figure S6: Change in two probe conductance of device B when it is sourced from (a) the x direction and (b) the y direction of the Hall-bar sample, in an in-plane magnetic field with the same magnitude of $|B_{\parallel}| = 1\,\mathrm{T}$ but pointing to the direction indicated by the polar angle. The carrier density is taken at five different values in the underdoped region of the p-side superconducting dome (see Fig. 4C for reference of what those carrier densities correspond to in the phase diagram).

field we can apply ($1\,\mathrm{T}$ in any in-plane direction). The resistivity is universally small up to $B_{\parallel} = 1\,\mathrm{T}$ and thus preventing us from extracting the magnitude and axis of the anisotropy. However, the nematicity at these densities near optimal doping can still be demonstrated if we reduce the superconducting gap size by either raising the temperature or applying a small perpendicular field, so that we could reach the critical magnetic field within $1\,\mathrm{T}$. Fig. S7 shows such experiments performed in device B. In both cases of Fig. S7a and b, when temperature is at base and no perpendicular field is applied (the lowest and darkest curve in each plot), the resistivity is very low (close to the instrumentation noise floor) and does not exhibit significant anisotropy with respect to θ_B. However if we raise the temperature (Fig. S7a) or apply a small perpendicular magnetic field (Fig. S7b) so that the superconductivity is partially suppressed, we can then observe the two-fold anisotropy versus θ_B.

In Fig. S8, we overlay the extracted nematicity temperature T_{nem} on top of the superconducting critical temperature T_c (at $10\,\%$ normal resistance). To obtain T_{nem} versus density, we set a threshold for the anisotropy magnitude of $A_{\mathrm{th}} = 0.1$ and find the carrier density that satisfies the condition $A = A_{\mathrm{th}}$ at each of the measured temperatures (no carrier density is found at $4\,\mathrm{K}$ satisfying this condition). The anisotropy in the ellipses would be barely visible if $A < A_{\mathrm{th}}$.

From this plot, it is evident that the nematicity essentially persists as long as the supercon-

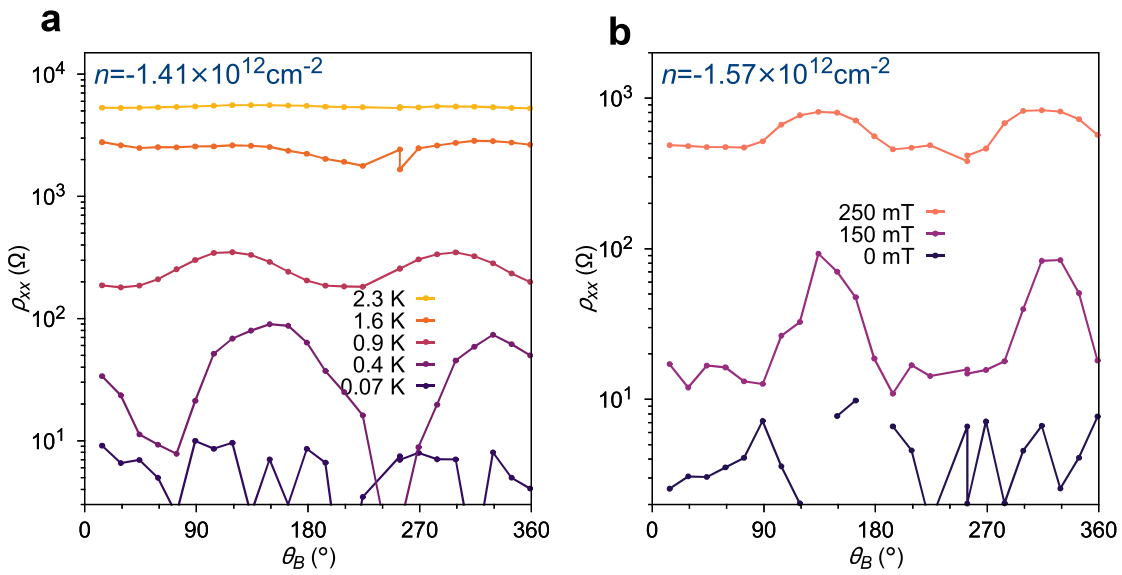

Figure S7: Nematicity as a function of temperature and perpendicular magnetic field in device B. The curves are the resistivity as a function of in-plane field direction θ_B, as (a) temperature is raised or (b) a small perpendicular field is applied. The in-plane field magnitude is fixed at at $|B_\parallel| = 1\,\mathrm{T}$. In (a), the perpendicular field is zero and in (b), the temperature is at the lowest temperature $70\,\mathrm{mK}$.

ductivity still exists. At several points, T_{nem} is even higher than $T_c^{10\%}$, which we attribute to the broad superconducting transition at these densities. We find that varying the threshold A_{th} will slightly change the shape of the T_{nem} curve, but our conclusion that T_{nem} roughly follows T_c remains unchanged.

3.8 In-plane Field Response at the Wedge-like Feature

In the main text, we discussed two types of broken rotational symmetry phases: anisotropic resistivity at the wedge-like feature above the superconducting dome, as well as the nematicity in the superconducting state. We argue that these two phases are distinct and might have different origins. To see this, we show the in-plane field nematicity measurements at two points inside the wedge-like feature in Fig. S9. At both points in the phase diagram, we cannot observe significant modulation of the resisitivity by the in-plane magnetic field, albeit the resistivity tensor of the similar device A has been shown to exhibit siginificant anisotropy inside the wedge-like feature right above the superconducting transition. This result indicates that an anisotropic resistivity tensor does not necessarily give rise to anisotropic response to the in-plane field in the normal state. The *vice versa* case is also true from the measurements we have shown in Fig. 5A and 5B: anisotropic response to the in-plane field can occur at a point in the phase diagram that

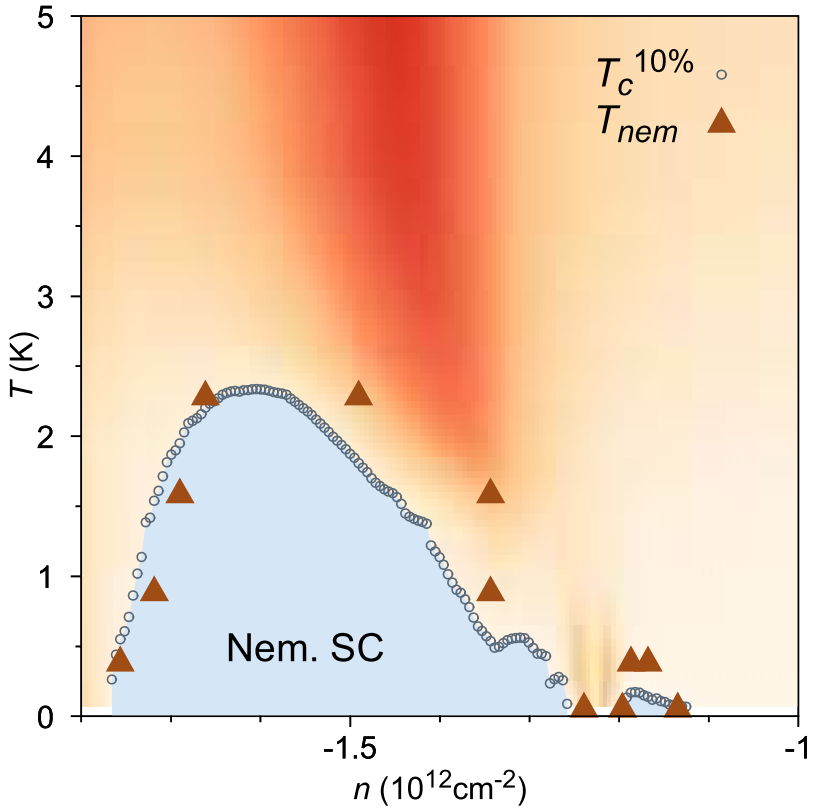

Figure S8: Nematicity temperature $T_{\rm nem}$ overlaid on the superconducting dome. The color map is the same data presented in Fig. 2B in the normal state for showing the position of the wedge-like feature and correlated insulator state.

does not exhibit normal-state anisotropy.

4 Additional Anisotropy Data

In this section, we present additional data that we measured in the normal state and superconducting anisotropy of MATBG. In particular, in device C with a twist angle of $(1.07 \pm 0.02)^\circ$ (see Table S1), which is very close to device A and B shown in the main text, we also find a similar 'wedge'-like feature on the underdoped side of the superconducting dome, as well as nematicity in the superconducting state. Fig. S10 shows the normal state anisotropy and nematic superconductivity in device C. Between $-1.5 \times 10^{12}\,\mathrm{cm}^{-2}$ and $-1.4 \times 10^{12}\,\mathrm{cm}^{-2}$, we find the 'wedge'-like resistive state, which has a significant anisotropy as manifested in the transverse voltage measurement. Remarkably, this 'wedge' fully suppresses superconductivity in the small density range where it is present, compared to the partial suppression of T_c in devices A and

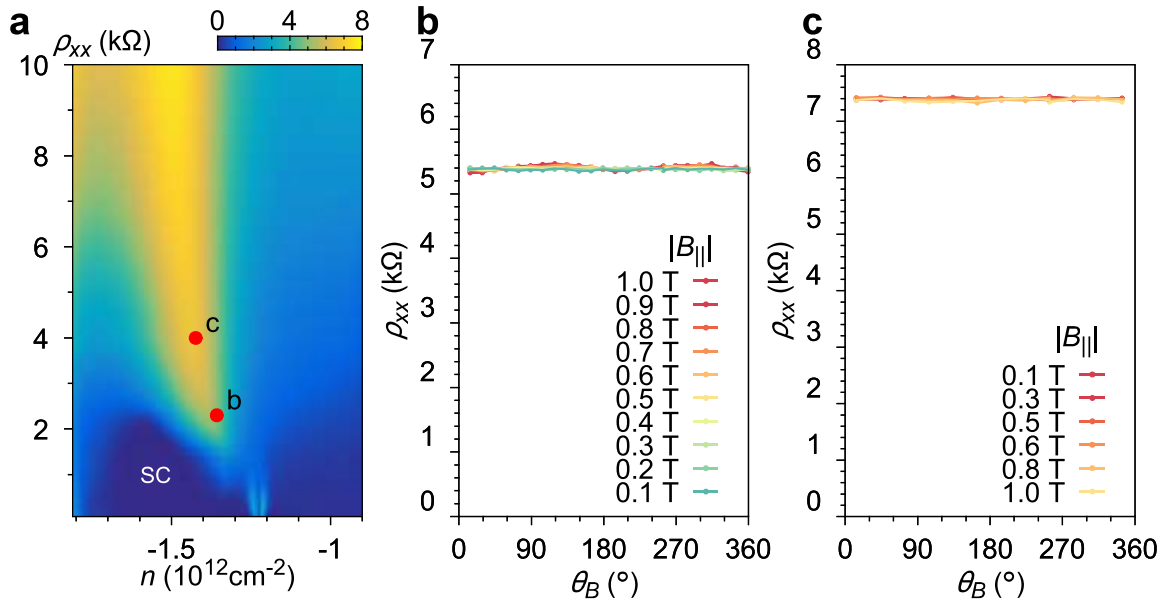

Figure S9: In-plane field response in the wedge-like feature in device B. Curves in (b) and (c) are the resisitivity versus in-plane field orientation and magnitude at two different points in the phase diagram, as indicated in (a). In both cases, we find no prominent two-fold symmetry in the in-plane field response.

B. In a small magnetic field, the 'wedge' feature turns into an insulator, similarly to the other devices. Devices A,B,C are the only devices in which we have found clear evidence for the 'wedge'-like feature, and they all lie within the narrow range of twist angles $(1.07 \pm 0.03)^\circ$. In addition, during the prepration of this manuscript we became aware of Ref. [58], in which two of their MATBG devices (device 2 and device 3 at $(1.04 \pm 0.02)^\circ$ and $(1.09 \pm 0.02)^\circ$ respectively) with close-by twist angles also showed similar resistive wedge features in the n-T phase diagram. Therefore, we believe that the normal-state anisotropy in the 'wedge' region is a distinct feature of MATBG that occurs when the twist angle is in the range of about $(1.07 \pm 0.03)^\circ$.

On the other hand, the nematic superconductivity appears to be a more ubiquitous phenomena across the entire range of twist angles where superconductivity emerges. Fig. S11 shows the H_{c2} anisotropy, similar to Fig. 4E to 4R, measured at representative densities in devices M7 (device A), M12, M1, and M2, respectively. As can be seen, all these devices exhibit nematicity, albeit their twist angles span from 0.95° to 1.16°. By observing nematic superconductivity in total six devices across the wide range of twist angles, we conclude that the nematicity is more likely to be intrinsic to the superconductivity, as opposed to present for only a small range of twist angles. We believe that the nematic symmetry of the pairing state component should be taken into consideration for understanding the superconducting order parameter of MATBG in general.

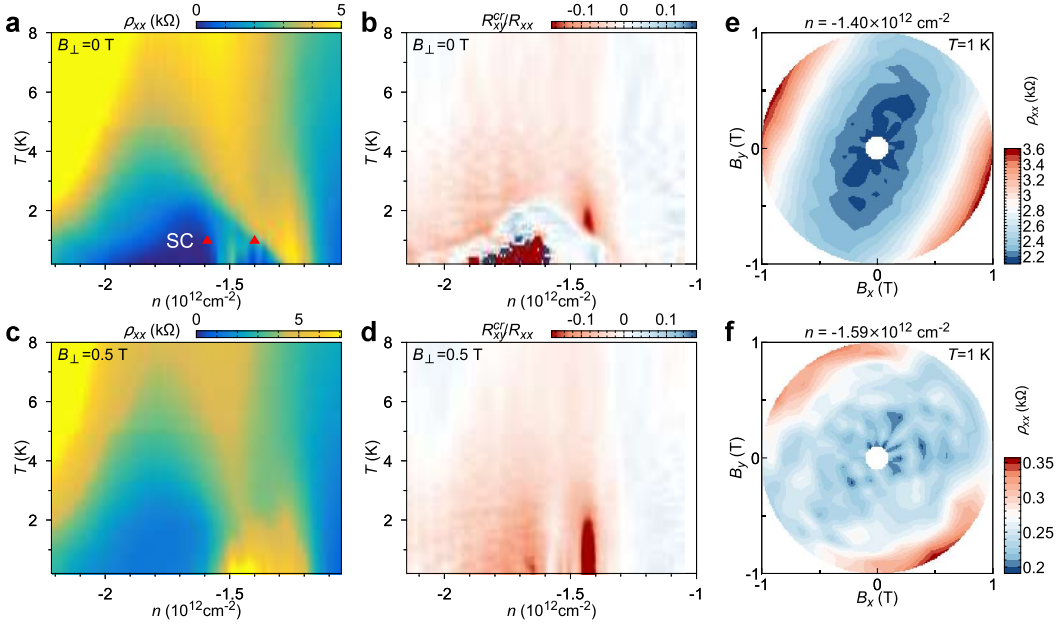

Figure S10: Anisotropy in device C with a twist angle of $1.07°$. (a-b) ρ_{xx} and R_{xy}^{cr} measured in device C as a function of n and T. An anisotropic 'wedge'-like feature is observed between $-1.5 \times 10^{12}\,\mathrm{cm}^{-2}$ and $-1.4 \times 10^{12}\,\mathrm{cm}^{-2}$, which fully suppresses the superconductivity in this density range. (c-d) Same measurements as in (a-b) but in $B_\perp = 0.5\,\mathrm{T}$. (e-f) Nematic superconductivity measured at the red triangles indicated in (a).

5 Phenomenological analysis of the nematicity

The Ginzburg-Landau free-energy density for a superconducting order parameter $\mathbf{\Delta} = (\Delta_1,\, \Delta_2)$ that transforms as the E representation (i.e. d-wave/p-wave) of the D_3 space group is given by [59]:

$$
\begin{aligned}
f_{\mathrm{SC}} = {} & r\left(|\Delta_1|^2 + |\Delta_2|^2\right) + \frac{u}{2}\left(|\Delta_1|^2 + |\Delta_2|^2\right)^2 \\
& + K_1\left|\partial_x\Delta_1 + \partial_y\Delta_2\right|^2 + K_2\left|\partial_x\Delta_2 - \partial_y\Delta_1\right|^2 + \frac{K_3}{2}\left[\left|\partial_x\Delta_1 - \partial_y\Delta_2\right|^2 + \left|\partial_x\Delta_2 + \partial_y\Delta_1\right|^2\right] \\
& - \frac{g}{2}\left[\left(|\Delta_1|^2 - |\Delta_2|^2\right)^2 + \left(\Delta_1\Delta_2^* + \Delta_1^*\Delta_2\right)^2\right] + \frac{w}{3}\left[\left(\Delta_1 + i\Delta_2\right)^3\left(\Delta_1^* + i\Delta_2^*\right)^3 + \mathrm{h.c.}\right]
\end{aligned}
\tag{4}
$$

Here, $r \propto T - T_{c,0}$, where $T_{c,0}$ is the mean-field superconducting transition temperature; K_i is a superconducting stiffness; $g > 0$ ensures that the ground state is the nematic one, i.e. $\mathbf{\Delta} = \Delta\left(\cos\theta_s,\, \sin\theta_s\right)$; $u > g$ ensures that the functional is bounded; and the sixth-order term restricts θ_s to three values (modulo-π). The superconducting nematic order parameter $\mathbf{\Phi}_s =$

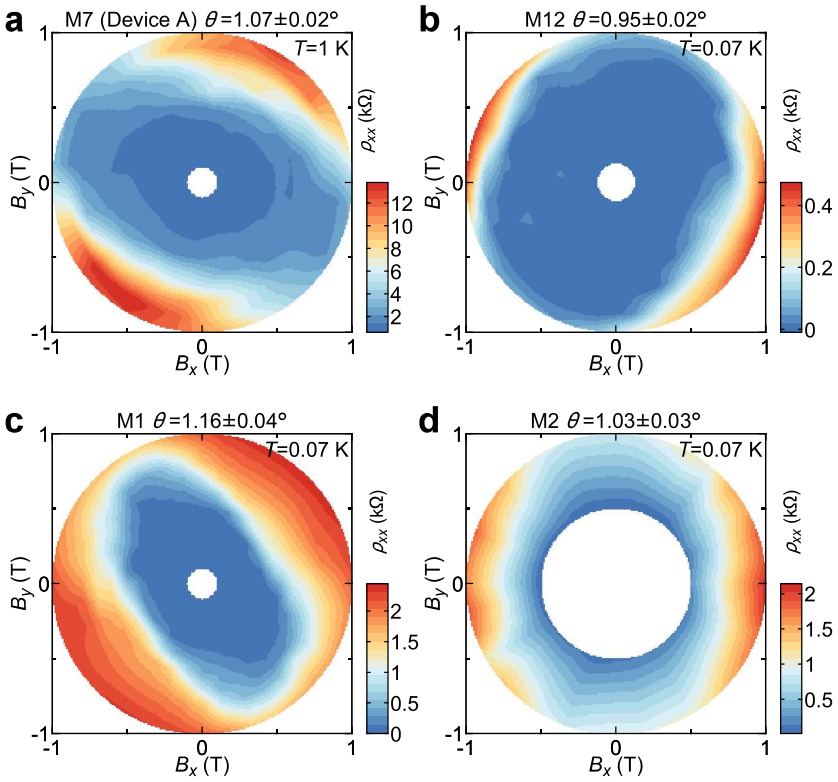

Figure S11: Nematic superconductivity in devices M7 (device A), M12, M1, M2. Each plot shows the resistivity versus in-plane magnetic field at a representative density in their respective superconducting domes.

$(\Phi_{1,s},\, \Phi_{2,s})$ arises as a composite order parameter – for instance, by performing a Hubbard-Stratonovich decoupling of the quartic term that has the coefficient g [41, 14]:

$$\begin{aligned} \Phi_{1,s} &= g\left(|\Delta_1|^2 - |\Delta_2|^2\right) \\ \Phi_{2,s} &= g\left(\Delta_1 \Delta_2^* + \Delta_1^* \Delta_2\right) \end{aligned} \tag{5}$$

As discussed elsewhere [41, 14], $\mathbf{\Phi}_s$ can spontaneously order on its own and give rise to a vestigial nematic phase, i.e. a phase where $\langle \mathbf{\Phi}_s \rangle \neq 0$ but $\langle \Delta_i \rangle = 0$. In our case, since strain is assumed to be present, one expects $\mathbf{\Phi}_s$ to be non-zero above T_c. This not only selects $\mathbf{\Delta} = \Delta\left(\cos\theta_s,\, \sin\theta_s\right)$ as the ground state, but it also gives rise to the following term in the free energy:

$$f_{\text{coupl}} = -\Phi_s \Delta^2 \cos\left(2\theta_s - 2\theta_s'\right) \tag{6}$$

where we parametrized $\mathbf{\Phi}_s = \Phi_s\left(\cos 2\theta_s', \sin 2\theta_s'\right)$. Minimization of this term gives $\theta_s = \theta_s'$, i.e. the relative amplitude of the two components of $\mathbf{\Delta}$ in the ground state is determined by the superconducting nematic director θ_s', which is set above T_c in the presence of strain.

By fixing the value of θ_s, one obtains an anisotropic superconducting susceptibility χ_s. The latter can be readily obtained from the quadratic terms in Eq. (4). Performing a Fourier transformation, we find:

$$\chi_s^{-1}\left(\mathbf{q}\right) = A\left[r + K_0 q^2 + \bar{K} q^2 \cos\left(2\theta_s - 2\varphi\right)\right] \tag{7}$$

where $K_0 \equiv \frac{K_1+K_2+K_3}{2}$, $\bar{K} \equiv \frac{K_1-K_2}{2}$, $A > 0$ is a constant, and $\tan\varphi = q_y/q_x$. Now, as argued in the main text, because orbital effects are expected to be significant even in the presence of an in-plane magnetic field, we assume that the anisotropy in H_c can be related to the anisotropy of the superconducting susceptibility. Since the contours of Eq. (7) give ellipses that make an angle θ_s with respect to the q_x axis, we therefore expect that measurements of the in-plane H_c will also produce ellipses oriented according to the angle θ_s. This reasoning is similar to that proposed in Ref. [40] to explain the observed critical field anisotropy in doped Bi_2Se_3 – note, however, that in that case the critical field is given simply by H_{c2}.

We now discuss how θ_s is affected by uniaxial strain applied along an axis rotated α with respect to the x axis. We focus on the free energy of the composite order parameter $\mathbf{\Phi}_s = \Phi_s\left(\cos 2\theta_s', \sin 2\theta_s'\right)$; since $\theta_s = \theta_s'$, we will drop the prime hereafter. Following the results of Ref. [39], the free energy of the nematic superconducting order parameter in the presence of strain ε is:

$$f_{\text{nem}} = \frac{a}{2}\Phi_s^2 + \frac{u}{4}\Phi_s^4 + \frac{\gamma}{3}\Phi_s^3\cos 6\theta_s - \lambda\varepsilon\Phi_s\cos\left(2\theta_s - 2\alpha\right) \tag{8}$$

Here, $a,\ u,\ \gamma,\ \lambda$ are phenomenological parameters. Note that γ selects three possible values for θ_s (modulo-π): $\gamma > 0$ chooses $\theta_s = \frac{\pi}{6},\ \frac{\pi}{2},\ \frac{5\pi}{6}$, whereas $\gamma < 0$ chooses $\theta_s = 0,\ \frac{\pi}{3},\ \frac{2\pi}{3}$. Hence, $\mathbf{\Phi}_s$ is a 3-state Potts model order parameter.

The key point, as discussed in Ref. [39], is that if the system is in the nematic disordered state ($a > 0$), we can restrict the free-energy analysis to the quadratic level and minimize it with respect to θ_s and Φ_s, finding either $\theta_s = \alpha$ (if $\lambda\varepsilon > 0$) or $\theta_s = \frac{\pi}{2} + \alpha$ (if $\lambda\varepsilon < 0$). Thus, if the anisotropy in H_c seen in the experiment was caused solely by strain, we would expect it to be unchanged as function of doping, since $\lambda\varepsilon$ is a property of the device.

The situation changes if the nematic order parameter is not simply induced by the strain, but would spontaneously onset even in the absence of strain. In this case, as discussed in Ref. [39], one can approximate Φ_s by a constant Φ_0 and minimize the last two terms of the free energy (8) with respect to θ_s:

$$\sin 6\theta_s = \left(\frac{\lambda\varepsilon}{\gamma\Phi_0^2}\right)\sin\left(2\theta_s - 2\alpha\right) \tag{9}$$

The result is that, depending on the relative sign between γ and $\lambda\varepsilon$, the angle θ_s will change as the magnitude of the nematic order parameter Φ_0 changes. A changing Φ_0 is presumably

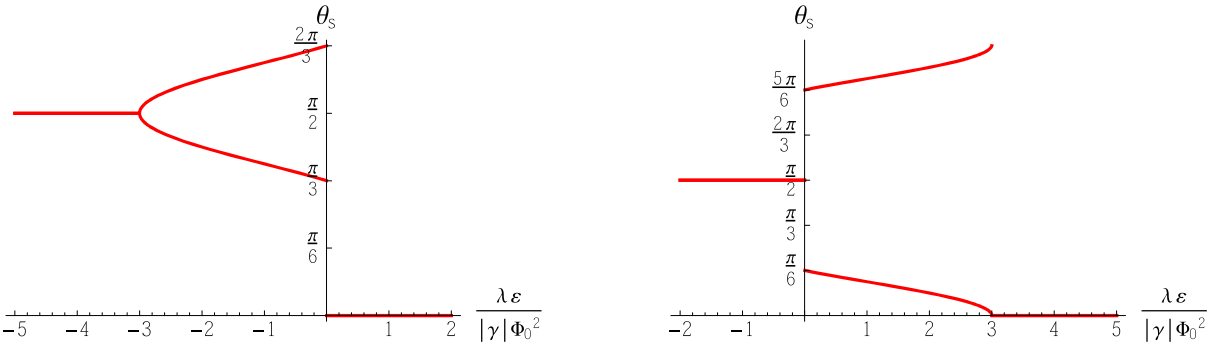

Figure S12: Superconducting nematic director θ_s as function of the normalized strain parameter $\frac{\lambda\varepsilon}{|\gamma|\Phi_0^2}$ for the cases $\gamma < 0$ (left panel) and $\gamma > 0$ (right panel). Here, $\alpha = 0$, i.e. strain is applied along the x axis.

what happens as the superconducting dome is traversed by varying the doping concentration.

For concreteness, let us consider the simpler case in which the strain is applied along one of the high-symmetry directions of the moiré superlattice, say $\alpha = 0$. Fig. S12 shows the solution of Eq. (9) as function of the parameter $\frac{\lambda\varepsilon}{|\gamma|\Phi_0^2}$ for fixed $\gamma < 0$ (left panel) and fixed $\gamma > 0$ (right panel). In the left panel, we see that when $\lambda\varepsilon > 0$, θ_s is pinned at 0 for any value of Φ_0. However, when $\lambda\varepsilon < 0$, θ_s rotates from $\pi/2$ to either $\pi/3$ or $2\pi/3$ as Φ_0 increases. The right panel illustrates the corresponding behavior for $\gamma > 0$. Thus, the experimental observation that θ_s rotates as a function of doping provides strong evidence in favor of the scenario in which the superconducting nematic order would be present even in the absence of strain. In this regard, strain is selecting a nematic domain rather than being the driving force behind the anisotropy.

While a complete description of the experimental observations regarding the doping dependence of θ_s is beyond the scope of our phenomenological approach, it is interesting to further discuss what can cause the rapid rotation of θ_s in the doping range $-1.45 \times 10^{12}\,\mathrm{cm}^{-2}$ to $-1.25 \times 10^{12}\,\mathrm{cm}^{-2}$(Figs. 4I to 4M in the main text). This is the same region of the phase diagram where the wedge-like feature intercepts the superconducting dome. As explained in the main text, the wedge-like state has a nematic component $\mathbf{\Phi}_n = \Phi_n\,(\cos 2\theta_n,\, \sin 2\theta_n)$. This nematic component, which is presumably independent from the superconducting nematic order parameter $\mathbf{\Phi}_s$, couples to the latter in a similar way as strain does:

$$\tilde{f}_{\mathrm{nem}} = -\tilde{\lambda}\Phi_n\Phi_s\cos\left(2\theta_s - 2\theta_n\right) \tag{10}$$

Now, if θ_n is alligned with the strain direction for all temperatures, then Φ_n combines with ε to form an effective strain $\varepsilon_{\mathrm{eff}} = \varepsilon + \frac{\tilde{\lambda}}{\lambda}\Phi_n$. Thus, if $\tilde{\lambda}$ and λ have opposite signs, a finite Φ_n could cause a sign change in $\lambda\varepsilon_{\mathrm{eff}}$. This in turn would cause θ_s to jump from 0 to $\pi/3$ (or from π to $2\pi/3$), and then rotate continuously towards $\pi/2$, as shown in the left panel of Fig. S12 . Of course, if the strain is not precisely aligned with one the high-symmetry directions, the jump would be replaced by a smooth behavior. It is interesting that this sequence of rotations seems

to be realized in the doping range $-1.45 \times 10^{12}\,\mathrm{cm}^{-2}$ to $-1.25 \times 10^{12}\,\mathrm{cm}^{-2}$, where normal-state and superconducting nematicities coexist. As shown in Figs. 4I to 4M of the main text (see also Fig. 6), starting from the highest doping concentration and moving towards $-n_s/2$, the major axis of the H_c ellipse seems to rotate by $\pi/2$. It would be interesting to perform STM measurements to further map the orientation of the nematic director and correlate it with residual strains present in the device.

This analysis reveals how the nematic order parameter associated with the wedge-like feature, $\mathbf{\Phi}_n$, affects the director of the superconducting nematic ground state. More generally, $\mathbf{\Phi}_n = (\Phi_{n,1},\, \Phi_{n,2})$ couples to $\mathbf{\Delta} = (\Delta_1,\, \Delta_2)$ in two rather distinct ways. Symmetry considerations restrict the Landau free-energy expansion to:

$$f_{\mathrm{SC-nem}} = \alpha_1 \left(\Phi_{n,1}^2 + \Phi_{n,2}^2\right) \left(|\Delta_1|^2 + |\Delta_2|^2\right) + \alpha_2 \left[\Phi_{n,1} \left(|\Delta_1|^2 - |\Delta_2|^2\right) + \Phi_{n,2} \left(\Delta_1 \Delta_2^* + \Delta_1^* \Delta_2\right)\right] \tag{11}$$

The first term is just the standard biquadratic coupling between ordered states that break different symmetries. The second term, which is essentially just a rewritten form of Eq. (10), is a linear-quadratic coupling that reflects the fact that the two ordered states share one similar broken symmetry, namely, three-fold rotations. The first term implies phase competition when $\alpha_1 > 0$, since nematic order would cause a suppression in the superconducting T_c. One of the effects of the second term is to correlate the nematic directors of the wedge-like feature and of the superconducting state, as discussed above. However, even when there is no long-range nematic order in the normal state – i.e. outside the wedge-like region in the phase diagram – this term can significantly impact the nature of the superconducting ground state. In this regime, one can integrate out the Gaussian normal-state nematic fluctuations and obtain the following contribution to the superconducting free energy:

$$\tilde{f}_{\mathrm{SC}} = -\frac{\alpha_2^2 \chi_{\mathrm{nem}}}{2} \left[\left(|\Delta_1|^2 - |\Delta_2|^2\right)^2 + \left(\Delta_1 \Delta_2^* + \Delta_1^* \Delta_2\right)^2\right] \tag{12}$$

Here, χ_{nem} is the nematic susceptibility associated with the wedge-like feature. Comparing to Eq. (4), we conclude that the normal-state nematic fluctuations favor the nematic ground state, as opposed to the time-reversal symmetry-breaking ground state ($p + ip$ or $d + id$) that would be favored if $g < 0$ in Eq. (4). A similar effect was identified in tetragonal systems with nearly-degenerate s-wave and d-wave superconducting instabilities in Ref. [57]. Similarly, Ref. [38] found that unidirectional charge-density wave fluctuations also favor a nematic superconducting ground state. Indeed, in the case where the wedge-like feature is associated with charge density-wave order, Φ_n can be expressed as a composite charge order parameter.